

3-10-2010

CFD Analysis of Experimental Wing and Winglet for FalconLAUNCH 8 and the ExFIT Program

Benjamin P. Switzer

Follow this and additional works at: <https://scholar.afit.edu/etd>

 Part of the [Aerodynamics and Fluid Mechanics Commons](#), and the [Space Vehicles Commons](#)

Recommended Citation

Switzer, Benjamin P., "CFD Analysis of Experimental Wing and Winglet for FalconLAUNCH 8 and the ExFIT Program" (2010).
Theses and Dissertations. 2056.
<https://scholar.afit.edu/etd/2056>

This Thesis is brought to you for free and open access by the Student Graduate Works at AFIT Scholar. It has been accepted for inclusion in Theses and Dissertations by an authorized administrator of AFIT Scholar. For more information, please contact richard.mansfield@afit.edu.



**CFD ANALYSIS OF EXPERIMENTAL WING AND WINGLET
FOR FALCONLAUNCH 8 AND THE EXFIT PROGRAM**

THESIS

Benjamin P. Switzer, Second Lieutenant, USAF

AFIT/GAE/ENY/10-M25

**DEPARTMENT OF THE AIR FORCE
AIR UNIVERSITY**

AIR FORCE INSTITUTE OF TECHNOLOGY

Wright-Patterson Air Force Base, Ohio

APPROVED FOR PUBLIC RELEASE; DISTRIBUTION UNLIMITED

The views expressed in this thesis are those of the author and do not reflect the official policy or position of the United States Air Force, Department of Defense, or the United States Government.

This material is declared a work of the U.S. Government and is not subject to copyright protection in the United States.

AFIT/GAE/ENY/10-M25

CFD ANALYSIS OF EXPERIMENTAL WING AND WINGLET
FOR FALCONLAUNCH 8 AND THE EXFIT PROGRAM

THESIS

Presented to the Faculty

Department of Aeronautics and Astronautics

Graduate School of Engineering and Management

Air Force Institute of Technology

Air University

Air Education and Training Command

In Partial Fulfillment of the Requirements for the
Degree of Master of Science in Aeronautical Engineering

Benjamin P. Switzer, B.S.

Second Lieutenant, USAF

March, 2010

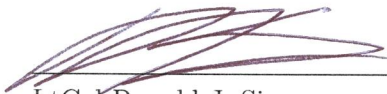
APPROVED FOR PUBLIC RELEASE; DISTRIBUTION UNLIMITED

AFIT/GAE/ENY/10-M25

CFD ANALYSIS OF EXPERIMENTAL WING AND WINGLET
FOR FALCONLAUNCH 8 AND THE EXFIT PROGRAM

Benjamin P. Switzer, B.S.
Second Lieutenant, USAF

Approved:



LtCol Ronald J. Simmons
Thesis Advisor

16 Mar 10

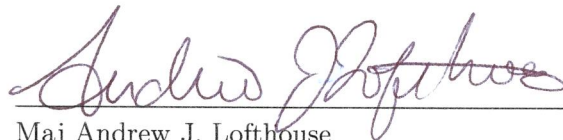
Date



Dr. Jonathan T. Black
Committee Member

16 MAR 2010

Date



Maj Andrew J. Lofthouse
Committee Member

16 Mar 10

Date

Abstract

Reusable launch vehicles have many benefits over their expendable counterparts. These benefits range from cost reductions to increased functionality of the vehicles. Further research is required in the development of the technology necessary for reusable launch vehicles to come to fruition. The Air Force Institute of Technology's future involvement in the ExFIT program will entail designing and testing of a new wing tip mounted vertical stabilizer in the hypersonic regime. One proposed venue for experimentation is to utilize the United States Air Force Academy's FalconLAUNCH Program which annually designs, builds, and launches a sounding rocket capable of reaching hypersonic speeds. In the Spring of 2010 an experimental wing geometry will be flown on FalconLAUNCH VIII for the ExFIT Program. The following study outlines the Computational Fluid Dynamics analysis used to determine lift and drag characteristics as well as temperature distributions of the wing geometry before testing to produce a successful launch. A majority of this analysis focused on the effects caused by shock waves forming on the winglet and their impact on the lifting characteristics and temperature distribution of the wing. Ultimately a recommendation of a 3° angle of attack is given for the experimental wings on the rocket. At this configuration the lift and drag generated by the experimental wings will be at a minimum allowing for greater stability and speed throughout the flight of the rocket.

Acknowledgements

First, I need to thank God because my completion of this thesis and master's degree was nothing short of a miracle and my faith proved invaluable. Second my wife, surely you know I love you very much. Third is my thesis MVP, I couldn't have finished without you big guy. Fourth is my Brother Rat and fellow AFIT Warrior, thanks for being there bud. Next is the Linux lab crew, you guys made it bearable. Also my friends and family, the support was great and thank you. Finally I'd like to thank my advisor, my committee members, and all of my professors for doing their part.

Benjamin P. Switzer

Table of Contents

| | Page |
|---|------|
| Abstract | iv |
| Acknowledgements | v |
| Nomenclature | ix |
| List of Figures | xi |
| I. Introduction | 1 |
| 1.1 Motivation for Research | 1 |
| 1.2 Research Approach | 2 |
| 1.3 Outline of Thesis | 3 |
| II. Background Research | 4 |
| 2.1 X-20 Dyna-Soar Program | 4 |
| 2.2 Lifting Body Research and the Space Shuttle | 5 |
| 2.3 DARPA and the Blackswift Project | 6 |
| 2.4 HIFiRE Program | 7 |
| 2.5 FAST Program | 8 |
| 2.6 ExFIT and USAFA's FalconLAUNCH Program | 11 |
| III. Methodology and Theory | 13 |
| 3.1 Selection of Geometry and Placement | 13 |
| 3.2 Grid Generation | 14 |
| 3.2.1 Grid Generation Outline | 14 |
| 3.2.2 Database | 15 |
| 3.2.3 Connectors | 16 |
| 3.2.4 Nodes | 18 |

| | Page |
|-------|--|
| 3.2.5 | Domains 22 |
| 3.2.6 | Blocks 23 |
| 3.2.7 | Boundary Conditions 27 |
| 3.3 | Flight Profile Data Point Selection 28 |
| 3.4 | AVUS Code 29 |
| 3.4.1 | Job File 29 |
| 3.4.2 | Navier-Stokes Equation Set 29 |
| 3.4.3 | Spalart-Allmaras Turbulence Model 29 |
| 3.4.4 | Gottlieb and Groth Riemann Solver 30 |
| 3.5 | Grid Independence Check 31 |
| 3.6 | Finite Element Analysis 32 |
| 3.7 | Convergence Tests 32 |
| IV. | Results 33 |
| 4.1 | Lift and Drag Characteristics 33 |
| 4.1.1 | Lift Characteristics 35 |
| 4.1.2 | Drag Characteristics 42 |
| 4.2 | Shock-Shock Interactions and Temperature Distribution 43 |
| 4.3 | Angle of Attack for the Experiment 46 |
| 4.4 | Temperature Data Collection and Heating Issues 48 |
| V. | Conclusions and Recommendations 50 |
| 5.1 | Conclusions 50 |
| 5.2 | Recommendations and Suggestions for Future Research 50 |
| 5.2.1 | Changes in Gridding 50 |
| 5.2.2 | Changes to the Experiment 51 |
| VI. | Appendix-A: Flight Profile Data Points 52 |
| VII. | Appendix-B: Sample Job File 53 |

| | Page |
|---|------|
| VIII Appendix-C: Navier-Stokes Equations | 56 |
| IX. Appendix-D: Spalart Allmaras Turbulence Model Equations | 58 |
| X. Appendix-E: Gottlieb and Groth Riemann Solver | 59 |
| XI. Appendix-F: C_l vs Mach Number Plots | 61 |
| XII. Appendix-G: C_d vs Mach Number Plots | 63 |
| XIII Appendix-H: Raw Coefficient Data for 3° Angle of Attack | 66 |
| Bibliography | 67 |
| Vita | 69 |

Nomenclature

Symbols

| | |
|-------------|--|
| a | Speed of Sound |
| C_l | Coefficient of Lift |
| C_d | Coefficient of Drag |
| d | Distance to the Wall |
| d_t | Distance from a Field Point to the Surface |
| E | Total Energy |
| \vec{F}_c | Vector of Convective Flux |
| \vec{F}_v | Vector of Viscous Flux |
| H | Total Enthalpy |
| k | Thermal Conductivity |
| M | Mach Number |
| n | Unit Normal to Surface |
| P | Pressure |
| P^* | Common Pressure |
| R | Gas Constant of Air |
| S | Arbitrary Surface |
| t | Time |
| T | Temperature |
| u | Velocity in the x Direction |
| u^* | Common Velocity |
| v | Velocity in the y Direction |
| V | Contravariant Velocity |
| w | Velocity in the z Direction |
| \vec{W} | Vector of Conservative Variables |

Greek

| | |
|------------|---------------------------|
| α | Angle of Attack |
| α_o | Zero Lift Angle of Attack |
| γ | Ratio of Specific Heats |
| κ | Von Karman Constant |

| | |
|-------------|--|
| ν | Viscosity |
| ν_t | Turbulent Viscosity |
| $\bar{\nu}$ | Working Variable used in Spalart Allmaras |
| ω_t | Vorticity at the Surface |
| Ω | Arbitrary Control Volume |
| ρ | Density |
| τ | Viscous Stress Tensor |
| Θ | Work of Viscous Stresses and Heat Conduction |

Abbreviations

| | |
|---------|--|
| AFIT | Air Force Institute of Technology |
| AFRL | Air Force Research Laboratory |
| AFRL/RB | Air Force Research Laboratory Air Vehicles Directorate |
| AVUS | Air Vehicles Unstructured Solver |
| CFD | Computational Fluid Dynamics |
| DARPA | Defense Advanced Research Projects Agency |
| DTSO | Defense Science and Technology Organization |
| ExFIT | Experimental Fin Tip |
| FAST | Future responsive Access to Space Technologies |
| FL | FalconLAUNCH |
| HCV | Hypersonic Cruise Vehicle |
| HIFiRE | Hypersonic International Flight Research and Experimentation |
| MPI | Message Passing Interface |
| NACA | National Advisory Committee for Aeronautics |
| RBS | Reusable Booster System |
| SBIR | Small Business Initiative Research |
| SLV | Small Launch Vehicle |
| USAF A | United States Air Force Academy |

List of Figures

| Figure | | Page |
|--------|---|------|
| 1. | Solid drawing of the wing geometry | 3 |
| 2. | Proposed X-20 Aircraft [1] | 4 |
| 3. | Lifting Body Vehicles | 6 |
| 4. | Conceptual Design of the Blackswift Test Bed [2] | 7 |
| 5. | HIFiRE 0 Test Launch in May 2009 [3] | 8 |
| 6. | AFRL FAST Program Reference Flight System [4] | 9 |
| 7. | Artist Drawing of XCOR’s Sub-Orbital Lynx Vehicle [4] | 9 |
| 8. | Proposed Flight Profile for Virgin Galactic’s SpaceShipTwo Vehicle [5] | 10 |
| 9. | Solid drawing of the FLVII Experimental Fin | 11 |
| 10. | Solid drawing the Wing with Sensor Cut-Outs | 14 |
| 11. | Database foundation for the grid | 15 |
| 12. | Connectors built on the Database | 16 |
| 13. | Sheath Connectors | 16 |
| 14. | Elbow Section Connectors | 17 |
| 15. | Flat Plate Connectors | 17 |
| 16. | Upstream Connectors | 18 |
| 17. | Nodes on the Leading and Trailing Edge Connectors | 19 |
| 18. | Nodes on the Main Wing Root and Winglet Tip | 19 |
| 19. | Nodes on the Elbow Connectors | 20 |
| 20. | Nodes on the Sheath, Elbow, and Part of the Upstream Section Con- nectors | 20 |
| 21. | Nodes on the Upstream and Flat Plate Connectors | 21 |
| 22. | Nodes on the Farfield Connectors | 21 |
| 23. | Domains on the Top and Bottom of the Wing | 22 |
| 24. | Domains on the Sheath, Elbow, Upstream and Flat Plate Sections of the Wing | 23 |

| Figure | | Page |
|--------|---|------|
| 25. | Domains on the Farfield and Symmetry Boundaries | 23 |
| 26. | Prismatic Block | 24 |
| 27. | Sheath Block | 24 |
| 28. | Elbow Enclosure Blocks | 25 |
| 29. | Upstream Blocks | 26 |
| 30. | The Farfield Block | 27 |
| 31. | Predicted FLVIII Flight Profile | 28 |
| 32. | Grid Independence Check | 31 |
| 33. | Typical Convergence Plot | 32 |
| 34. | C_l Against α for a Range of Reynolds Numbers | 33 |
| 35. | C_d Against α for a Range of Reynolds Numbers | 34 |
| 36. | $C_{l\alpha}$ vs Mach Number, Simulations | 35 |
| 37. | $C_{l\alpha}$ vs Mach Number, Bertin [6] | 35 |
| 38. | $\frac{L}{D_{max}}$ vs Mach Number, Simulations | 35 |
| 39. | $\frac{L}{D_{max}}$ vs Mach Number, Bertin [6] | 35 |
| 40. | C_l vs Mach Number $\alpha = 0^\circ$ | 36 |
| 41. | C_l vs Mach Number $\alpha = 1^\circ$ | 36 |
| 42. | C_l vs Mach Number $\alpha = 2^\circ$ | 36 |
| 43. | C_l vs Mach Number $\alpha = 3^\circ$ | 36 |
| 44. | C_l vs Mach Number $\alpha = 4^\circ$ | 37 |
| 45. | C_l vs Mach Number $\alpha = 5^\circ$ | 37 |
| 46. | C_l vs Mach Number $\alpha = 6^\circ$ | 37 |
| 47. | Winglet Shock Wave Development | 38 |
| 48. | Pressure Distribution of Upper and Lower Surfaces at Mach 2.0 and 2° | 39 |
| 49. | Pressure Distribution of Upper and Lower Surfaces at Mach 3.5 and 2° | 40 |
| 50. | Chordwise Pressure Contour Planes | 41 |
| 51. | C_d Against Mach Number at $\alpha = 2^\circ$ | 42 |

| Figure | | Page |
|--------|---|------|
| 52. | Temperature Distribution at $\alpha = 2^\circ$ | 43 |
| 53. | Temperature Contour Planes, 2° , Mach 4.5 | 45 |
| 54. | Combined Plane and Surface Temperature Contours, 2° , Mach 4.5 . . | 46 |
| 55. | C_l Against Mach Number at $\alpha = 3^\circ$ | 47 |
| 56. | C_d Against Mach Number at $\alpha = 3^\circ$ | 47 |
| 57. | Temperature Distribution at $\alpha = 3^\circ$ | 49 |
| 58. | C_l vs Mach Number $\alpha = 8^\circ$ | 61 |
| 59. | C_l vs Mach Number $\alpha = 10^\circ$ | 61 |
| 60. | C_l vs Mach Number $\alpha = 12^\circ$ | 61 |
| 61. | C_l vs Mach Number $\alpha = 14^\circ$ | 61 |
| 62. | C_l vs Mach Number $\alpha = 16^\circ$ | 62 |
| 63. | C_l vs Mach Number $\alpha = 18^\circ$ | 62 |
| 64. | C_l vs Mach Number $\alpha = 20^\circ$ | 62 |
| 65. | C_d vs Mach Number $\alpha = 3^\circ$ | 63 |
| 66. | C_d vs Mach Number $\alpha = 4^\circ$ | 63 |
| 67. | C_d vs Mach Number $\alpha = 3^\circ$ | 63 |
| 68. | C_d vs Mach Number $\alpha = 4^\circ$ | 63 |
| 69. | C_d vs Mach Number $\alpha = 5^\circ$ | 64 |
| 70. | C_d vs Mach Number $\alpha = 6^\circ$ | 64 |
| 71. | C_d vs Mach Number $\alpha = 8^\circ$ | 64 |
| 72. | C_d vs Mach Number $\alpha = 10^\circ$ | 64 |
| 73. | C_d vs Mach Number $\alpha = 12^\circ$ | 64 |
| 74. | C_d vs Mach Number $\alpha = 14^\circ$ | 64 |
| 75. | C_d vs Mach Number $\alpha = 16^\circ$ | 65 |
| 76. | C_d vs Mach Number $\alpha = 18^\circ$ | 65 |
| 77. | C_d vs Mach Number $\alpha = 20^\circ$ | 65 |

CFD ANALYSIS OF EXPERIMENTAL WING AND WINGLET
FOR FALCONLAUNCH 8 AND THE EXFIT PROGRAM

I. Introduction

Space exploration has been at the forefront of scientific research for over half a century. This research has evolved to a point in which access to space is relatively routine through the use of the Space Shuttle and expendable launch vehicles. However, the high cost and effort required by these methods places limits on the frequency of their use. The Future responsive Access to Space Technologies, or FAST, Program hopes to improve current methods used to reach space with new techniques and technology that will both increase frequency and reduce costs associated with space missions. The Experimental Fin Tip(ExFIT) Research Program supports the FAST Program by studying the behavior and performance of fin tips in the supersonic and low hypersonic regimes. The following research study documents the design and analysis of the 2010 ExFIT Program launch experiment. In this experiment the U.S. Air Force Academy's (USAFA) FalconLAUNCH (FL) Program will provide the test vehicle for data collection on a wing and fin tip that is based on the concept vehicles of the FAST Program. Data will be collected over the entire flight regime of the vehicle in one experiment, which will provide unique experimental data that is difficult to attain using wind tunnels. The following study outlines the Computational Fluid Dynamics (CFD) analysis used to determine lift and drag characteristics of the wing geometry before testing. This analysis reveals that shock waves forming on the main wing and winglet have a significant impact on the lifting characteristics as well as surface temperatures of the wing.

1.1 Motivation for Research

Research on platforms intended for economical, successive missions into space often exhibit similar wing geometry. Specifically, they utilize vertically mounted fin tips rather than a more conventional dorsal tail as the vertical stabilizers. Outboard vertical stabilizers have several advantages over dorsal stabilizers. First, at higher angles of attack these stabilizers will not be rendered useless by the wake of the fuselage, but will have more exposure

to free stream air. Second, in order for a dorsal tail to have any significant free stream airflow it must be much larger to avoid becoming ineffective due to the wake of the fuselage it requires a great deal of structural support within the vehicle. By removing the dorsal tail, the accompanying structural components in the vehicle are also discarded, eliminating weight and making the aft end of the vehicle more accessible for engine maintenance. Finally, stacking of equipment or additional stages becomes much easier[4].

Study of these types of wing and winglet combinations at the range of velocities anticipated has been limited. By utilizing the USAFA FL Program, experimentation of these wings can be conducted in conditions that closely resemble the flight profiles of the proposed reusable launch vehicles. Not only will this data encompass the entire profile expected for these vehicles, but it will all be collected in a single experiment. To replicate this amount of data without gaps in the flight profile through the use of wind tunnels would require the use of several tunnels and likely several different scale models. Furthermore, validation of FL as a practical means for collecting data on outboard vertical stabilizers will help establish the program as a viable platform for future ExFIT research projects.

1.2 Research Approach

The focus of this research is to obtain lift and drag characteristics for the FL vehicle by conducting a CFD analysis of the wing and winglet. These lift and drag profiles are strongly influenced by the interactions of the shock waves formed by the ExFIT experimental fins. Specifically, this shock interaction has a profound effect on coefficient of lift at high Reynolds numbers and low angles of attack. Though such interactions should be the focus of future studies, analysis of the experimental wing conducted here is sufficient to aid the USAFA in predicting launch trajectory and performance, and meeting launch requirements, including a 4Hz spin throughout the ascent.

To begin the CFD analysis, an unstructured grid is created using a scaled wing geometry that closely resembles the wings on current FAST concept vehicles, see Figure 1.

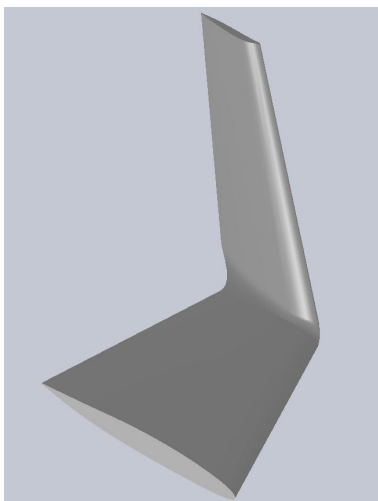


Figure 1 Solid drawing of the wing geometry

Next, using a predicted flight profile provided by the Academy, a set of flight conditions are selected to encompass the range of Mach numbers and altitudes the rocket will likely experience during the flight. These cases are then investigated using Air Vehicles Unstructured Solver (AVUS), a CFD code developed by the Air Force Research Laboratory Air Vehicles Directorate (AFRL/RB). For various points in the flight profile, the AVUS code will predict the coefficient of lift(C_l), coefficient of drag(C_d), overall lift, drag, span wise forces, as well as pitch, roll and yaw moments. A grid independence study is conducted to ensure the predictions outlined above do not have errors introduced by poor gridding. This data is then provided to USAFA to use in their own studies of rocket performance and safety.

1.3 *Outline of Thesis*

Chapter 2 discusses previous research regarding hypersonic vehicle testing and the use of vertically mounted wing tips. The following chapter describes the method used to grid the geometry, the theory used to develop the AVUS code, and the process to perform the CFD simulations. Chapter 4 provides a discussion of test results, and the final chapter contains conclusions drawn and recommendations for future research.

II. Background Research

Hypersonic vehicle projects date back as far as the 1950s and the X-20 Dyna-Soar Program. Eventually, these research efforts would evolve into a variety of projects such as the Space Shuttle, the Defense Advanced Research Projects Agency's (DARPA) Blackswift program, and recently the FAST and ExFIT Programs. This chapter details a chronological description of these programs and their research.

2.1 X-20 Dyna-Soar Program

The Dyna-Soar Program was started in 1957 to develop a vehicle capable of hypersonic speed and access to space. This research culminated in the X-20 conceptual aircraft. Like the FAST concept vehicle, the X-20 also used vertically-mounted wingtip stabilizers, as seen below in Figure 2.



Figure 2 Proposed X-20 Aircraft [1]

Initially, the goal was to develop a hypersonic military weapons system by progressing through three steps of research and testing. The first step was to develop a manned research vehicle that would gather aerodynamic and structural data at extremely high speeds and altitudes. This step would also be a basis for studying the effects of hypersonic high-altitude flight on the human body. Step two would see the evolution from a research vehicle to a manned high speed, high altitude, long range reconnaissance vehicle. The final phase would

pursue the overall program goal of an operational weapon system capable of orbital nuclear bombing, improved reconnaissance, and satellite identification and neutralization. Early in the program a letter to the Secretary of Defense, Robert S. McNamara, was written by the assistant secretary for research and development for Major General Osmond Ritland of the Ballistic Missile Division which summarized the goals and importance of the research effort[7].

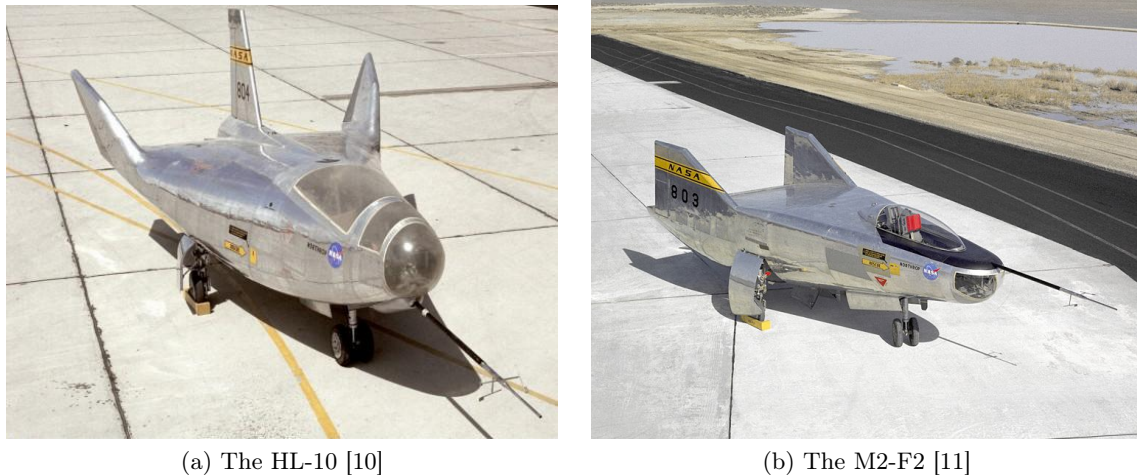
”The existing X-20 program will provide techniques for manned maneuverable re-entry and recovery, with the ability to initiate recovery at will, to land at a preselected base, to recover self-contained payloads for immediate examination and reuse, and to refurbish and reuse the spacecraft itself; all of which are essential to an economic and militarily sound space posture.” [8]

However, the Dyna-Soar Program was canceled shortly thereafter because the objective of the program was too narrow to justify the cost. Though the program was canceled before the vehicle could be built and tested, it created a foundation upon which future hypersonic testing and design programs could build. Many of the goals of the Dyna-Soar Program have been revisited by similar projects such as the lifting body, the Space Shuttle, DARPA’s Blackswift program, and the FAST Program[7].

2.2 Lifting Body Research and the Space Shuttle

The lifting body concept is another avenue taken by the National Advisory Committee for Aeronautics (NACA) in the early 50’s to further develop the concept of lifting rather than ballistic reentry from low Earth orbit. The work evolved from effects witnessed during the study of reentry survivable ballistic missile nose cones. Researchers found that blunting the nose of a missile created a shock wave that dissipated reentry energy much more effectively than a sharp nose. Further study concluded that a wingless half cone configuration would provide the high lift and drag necessary for optimal deceleration as well as allow for limited aerodynamic control. Many different aircraft, such as the M2-F1 and the HL-10 shown in Figure 3 were based on this concept. The results of testing on these vehicles laid the groundwork for the design of the Space Shuttle. Although these tests validated some of the FAST Program concepts, none of the tests done on these lifting body vehicles were in the

high supersonic or low hypersonic regime. For the entirety of testing, the HL-10 posted a maximum Mach number of 1.86 and a maximum altitude of 90,303ft[9].



(a) The HL-10 [10]

(b) The M2-F2 [11]

Figure 3 Lifting Body Vehicles

2.3 DARPA and the Blackswift Project

The Defense Advanced Research Projects Agency was founded in order to keep technology in the U.S. above the world curve. One of these projects is the FALCON Program, which was developed in 2003 to "develop and validate, in-flight, technologies that will enable both a near-term and far-term capability to execute time-critical, prompt global reach missions while at the same time, demonstrating affordable and responsive space lift." [12] To accomplish these tasks, from its inception the project set out to develop both a Hypersonic Cruise Vehicle (HCV) as well as a Small Launch Vehicle, or SLV. In the shorter term, the SLV would be designed to launch small satellites into low Earth orbit at low cost. The technology developed in the design of the SLV would transition into the long term HCV project. The proposed HCV would be able to take off from a conventional military runway and strike targets at a distance of up to 9,000 nautical miles in less than two hours. This technology would allow the U.S. to sustain a campaign from the continental U.S. while maintaining mission recall capability, which ballistic missiles do not have[13].

These aspirations developed into the Blackswift Test Bed, shown in Figure 4, which was a vehicle intended to test components necessary for hypersonic flight. In a DARPA

press release it was said that "Blackswift would have demonstrated key technologies such as efficient aerodynamic shaping for high lift to drag, lightweight and durable (reusable) high-temperature materials and thermal management techniques including active cooling, autonomous flight control, and turbine-based combined cycle propulsion." [13] However, as with the Dyna-Soar Program, funding for DARPA was reduced in FY 2009 and the Blackswift Test Bed was canceled before the aircraft could be built and tested[13].



Figure 4 Conceptual Design of the Blackswift Test Bed [2]

2.4 HIFiRE Program

The Hypersonic International Flight Research and Experimentation (HIFiRE) Program is an ongoing joint Program Arrangement between the Air Force Research Laboratory (AFRL) and the Australian Defense Science and Technology Organization (DTSO) to develop hypersonic systems. HIFiRE is investigating technologies required to achieve sustained hypersonic flight systems, including aeropropulsion, aerodynamics, aerothermodynamics, high temperature materials and structures, thermal management strategies, navigation, and control. The program will employ many different research approaches including CFD, ground simulation and experimentation, and flight testing. Furthermore, the HIFiRE Program will use sounding rockets similar to those built by the FL Program in order to launch payloads to hypersonic conditions, where data will be collected[14]. Flight testing began in May of 2009 with the launch of HIFiRE 0, which was a systems proving protoflight

for future tests (see Figure 5)[15]. Initially, HIFiRE set out to complete a series of up to 10 projects with each one culminating in a flight test. ExFIT hopes to perform hypersonic testing with FL in the same way that the HIFiRE Program employs sounding rockets.



Figure 5 HIFiRE 0 Test Launch in May 2009 [3]

2.5 *FAST Program*

The AFRL FAST Program is researching a vehicle that can persistently and reliably carry large payloads into space and return to Earth at low cost. In order to meet these goals they are pursuing designs for a Reusable Booster System, or RBS, that would be launched vertically, carry its payload of 1 to 41 klbm into space, and return to land horizontally at the launch site. Additionally, the vehicle should be able to fly a second mission within 48 hours of a previous mission. Based on these requirements the conceptual design shown in Figure 6 was created[4].

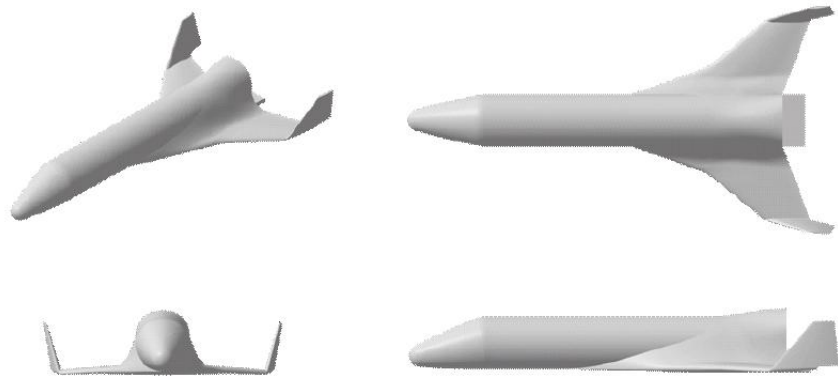


Figure 6 AFRL FAST Program Reference Flight System [4]

The concept vehicle incorporates a delta style wing with vertically mounted wing tip stabilizers, which provide the advantages of improved control at high angles of attack, reduced vehicle weight, ease of engine maintenance, and the ability to stack stages. Following this design, AFRL/RB awarded a Small Business Initiative Research (SBIR) contract to XCOR Aerospace to further the technology and demonstrate the capabilities of the FAST concept vehicle using XCOR's Lynx vehicle, shown in Figure 7. The Lynx vehicle was designed by XCOR as a vehicle for the space tourism industry and would fly passengers into space up to four times daily[4].



Figure 7 Artist Drawing of XCOR's Sub-Orbital Lynx Vehicle [4]

XCOR was chosen because they use a delta style wing and vertically mounted wing tip stabilizers which closely matches the FAST concept vehicle. Furthermore, the proposed flight profiles for each vehicle are also quite similar, although the Lynx vehicle takes off and lands horizontally. By granting XCOR a SBIR contract, the Air Force hoped to gain research data on the Lynx vehicle that could then be used to further efforts to develop an RBS. Data will be collected on vehicle-engine integration, reaction control system integration, composite structures, and highly responsive operations. Likewise, development of Lynx aeromechanics and a comparison of the methods used to analyze flight tests will advance the technology and knowledge base necessary for the creation of an RBS[4].

Furthermore, the Scaled Composites company has designed a vehicle called SpaceShipTwo for Virgin Galactic, which will be used for passenger space travel. This vehicle also shares a similar shape to the FAST vehicle using outboard vertical stabilizers. A picture of the SpaceShipTwo and its flight profile is shown in Figure 8[16]. Virginia Galactic's SpaceShipTwo and the Lynx vehicle highlight the need for the military to advance their technologies in the spaceflight arena or risk falling behind. Research in the ExFIT Program will help to foster this advancement.

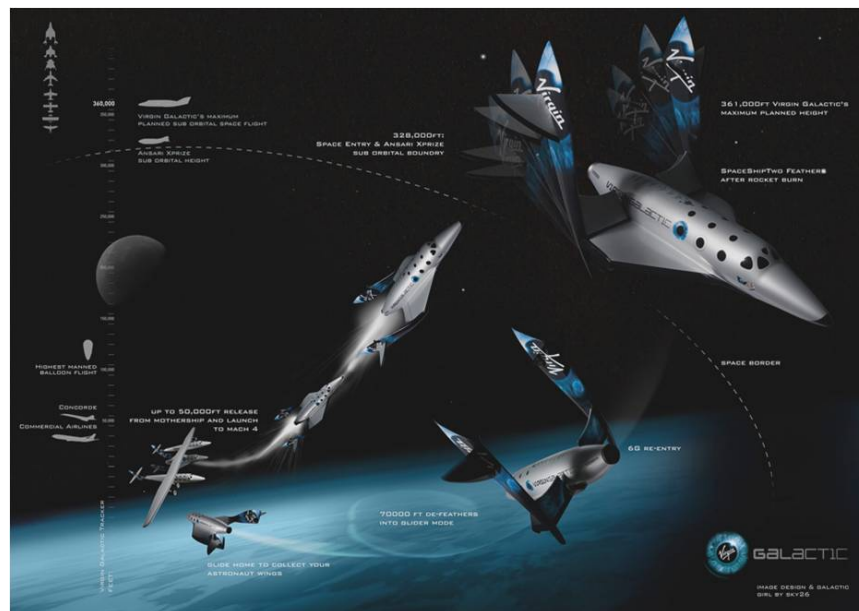


Figure 8 Proposed Flight Profile for Virgin Galactic's SpaceShipTwo Vehicle [5]

2.6 *ExFIT and USAFA's FalconLAUNCH Program*

To further ExFIT research, the Air Force Institute of Technology (AFIT) has been working closely with the USAFA and the FL Program to test vertically mounted wing tip stabilizers. The FL Program is a capstone design project in which senior cadets in the Astronautical Engineering Department at USAFA design and build a sounding rocket over the course of an academic year. This rocket provides AFIT with a platform capable of producing hypersonic speeds at relatively high altitudes, both of which are ideal characteristics for conducting experiments for the ExFIT Program. The program provides a unique and established platform for collecting data encompassing the entire flight profile of a proposed FAST vehicle in a single experiment. In addition, this will avoid problems wind tunnel testing presents, such as short test times, multiple scale models, and gaps in the data.

Prior to the current effort, AFIT worked with USAFA to examine possible causes and a solution for the failure of stabilizing fins on the fifth FL rocket, FLV. Joseph Simmons, a Masters student at AFIT conducted analysis of the FLV stabilization fins with an aeroelastic fin optimization tool[17]. He concluded that during the FLV flight, three of the four fins sheared off of the rocket due to aerodynamic flutter. This investigation of FLV aided the redesign of the stabilization fins which culminated in a successful FL VII launch.

The seventh FL rocket, FLVII, was the first to carry an ExFIT experiment as its payload. The experiment consisted of a 2.25 inch fin and cross tab outfitted with a strain gage (see Figure 9).



Figure 9 Solid drawing of the FLVII Experimental Fin

The intent was to demonstrate the capability to collect, store, and transmit data from the rocket. Strain data was to be gathered from the fin during the flight which reached a maximum speed of Mach 4.8 and a maximum altitude of 228 kft. This data was to be transmitted during flight from the rocket to a computer on the ground as well as recorded on the rocket itself. Once gathered, the data would be used to find the modal frequencies for this configuration throughout the flight profile. Due to a rocket computer power issue, no data was transmitted during flight. Furthermore, the rocket could not be recovered and no data from the experiment was obtained. Measures will be incorporated into future launches to ensure computer power during launch. An experiment using the wing geometry analyzed in this research study will be flown on the eighth FL rocket, FLVIII.

III. Methodology and Theory

Chapter 3 outlines the steps taken to complete the CFD analysis of the experimental wing and winglet to be flown on the eighth FL rocket, FLVIII. The first section discusses the process of selecting the geometry of the wing and winglet, as well as their placement on the rocket. The next sections describe the creation of the unstructured grid and boundary condition file, and also explain the process of selecting the flight profile data points and AVUS code parameters. The final sections outline the process by which grid independence is ensured and the method used to test the solutions for convergence.

3.1 Selection of Geometry and Placement

In order to obtain data relevant to both the ExFIT and FAST Programs the wing and winglet geometry was selected to resemble both the FAST concept and the Lynx vehicle. The geometry selected has a delta shaped main wing section with both aerodynamic and geometric twist, and a vertically mounted winglet sized proportionally for the main wing section. Once the overall geometry was established, placement of the wing on the rocket dictated the final dimensions.

Two possible locations for the experiment were considered; the first option was to use two smaller wings (approx. 3 inches), and place them at the front of the rocket on the nose cone. The second option was to utilize two of the experimental wings as aft stabilizers, along with two non-experimental stabilizers. The nose cone option will provide the wings with high speed, clean, free-stream air for data collection, but this also raises stability issues. Implementing the wings as two of the aft stabilizers will alleviate stability issues, but the air encountered by the wings will be moving at less than free-stream velocities and it will be turbulent. Ultimately, the latter option is chosen. Not only does the aft stabilizer option provide the rocket with added stability, but it also allows the wings themselves to be much larger than would be possible at the nose. The added size of the wings affords two advantages to the experiment. First, the effect of the rocket body turbulent boundary layer on the wings will be much smaller. Second, the data sample rate can be reduced because a larger specimen will have lower frequencies associated with the natural bending and torsional

modes. This reduces the size and complexity of the electronic systems required for data sampling and transmission. Figure 1, page 3, is a solid drawing of the wing geometry and Table 1 provides a list of the overall dimensions of the wing and winglet.

Table 1 Wing Geometry Dimensions (cm)

| Main Wing Section | | | | Winglet Section | | | |
|-------------------|-----------|-----------|-------------------|-----------------|-----------|-----------|-------------------|
| Root Chord | Tip Chord | Semi Span | Maximum Thickness | Root Chord | Tip Chord | Semi Span | Maximum Thickness |
| 24.4 | 10.9 | 17.5 | 1.9 | 10.9 | 6.1 | 14.9 | 0.66 |

The final geometry will be outfitted with two strain gages, as well as two temperature sensors. One strain gage and temperature sensor pair will be placed on the main wing section, and the other pair will be placed on the winglet. Figure 10 also shows the locations of these sensor pairs on the wing.

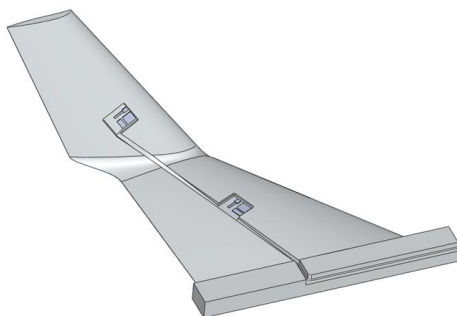


Figure 10 Solid drawing the Wing with Sensor Cut-Outs

3.2 Grid Generation

3.2.1 Grid Generation Outline. After finalizing the dimensions and position of the wing on the rocket, a 3D grid can be created which will divide the volume surrounding the wing geometry into several smaller volumes. However, before a grid can be generated a plan for the grid's layout must first be developed. This layout is based on the type of tests the grid is intended to solve. Because the tests would reach low hypersonic speeds, in this experiment the grid needed to capture the shock waves that the wing would develop during the simulations. Because of the configuration, shocks were expected to interact on top of the main wing near the winglet, referred to as the elbow. Therefore, a high density of cells was required in this area. A flat plate would be required in order to develop a boundary layer

similar to the one anticipated to grow on the rocket body. The wings would need to nearly zero lift during flight to ensure the non-experimental fins would provide a 4Hz spin required for range safety. Based on this need for near zero lift and because preliminary simulations showed zero lift would likely be at positive angles of attack all simulations will be at and above 0° . Therefore, cells will be focused in the upstream area of the grid corresponding to positive angles of attack. It was decided an unstructured grid, comprised of volumetric tetrahedral, pyramid, and prism cells was sufficient for this study and would be utilized for the research. An unstructured grid provides the level of accuracy necessary for the analysis while minimizing grid generation time[18].

3.2.2 Database. The first step in the grid generation process was opening the solid file of the finalized geometry in Gridgen, which is a program used to generate grids for CFD analysis. The wing solid file, once imported into Gridgen, could be used as a database. A database is a 3D template consisting of a group of points, curves or surfaces from which the entire grid can be built[18]. After adding a cylinder and two quarter sphere database sections around the wing as a farfield boundary, the gridding could begin. Figure 11 shows the wing and farfield database used in the creation of the final grid.

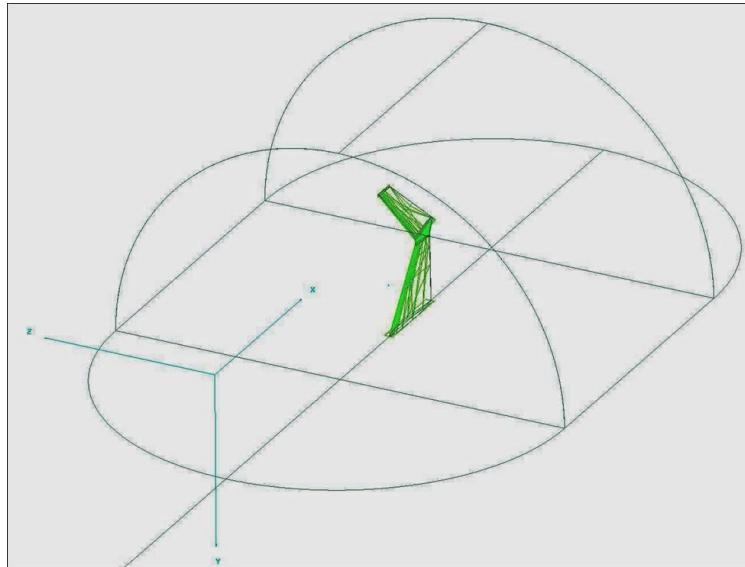


Figure 11 Database foundation for the grid

3.2.3 Connectors. Step two consisted of building the connectors, or lines on which the grid points are distributed, in both the database as well as within the volume[18]. These connectors are used to divide the volume into different surfaces, and eventually into different volumetric sections when cells are created. Connectors were first placed on the database entities defining the wing geometry as well as the farfield boundary (see Figure 12).

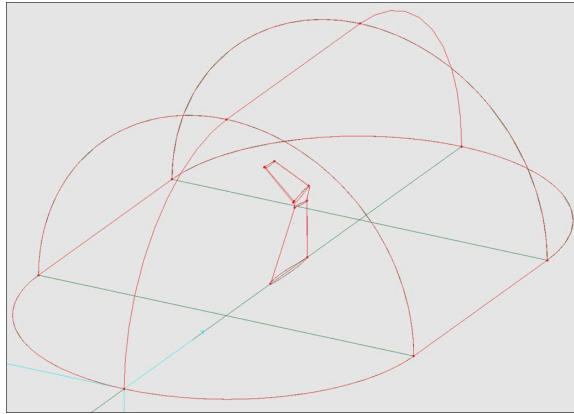


Figure 12 Connectors built on the Database

Next, the frame for a sheath surrounding the wing was constructed. This sheath ensured that the cell density remained high in the area directly surrounding the wing, which was capturing the shocks forming off the wing and winglet, see Figure 13.

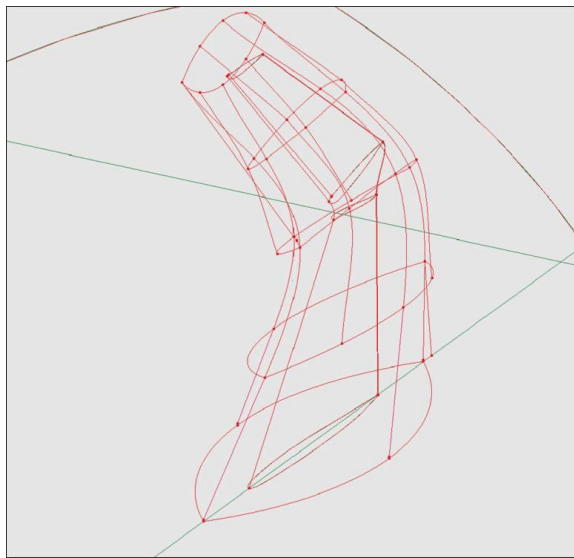


Figure 13 Sheath Connectors

Next, connectors that enclose the elbow of the wing were built; these provide the structure necessary to accommodate the number of cells needed to capture the shock interactions that will occur in that area, see Figure 14.

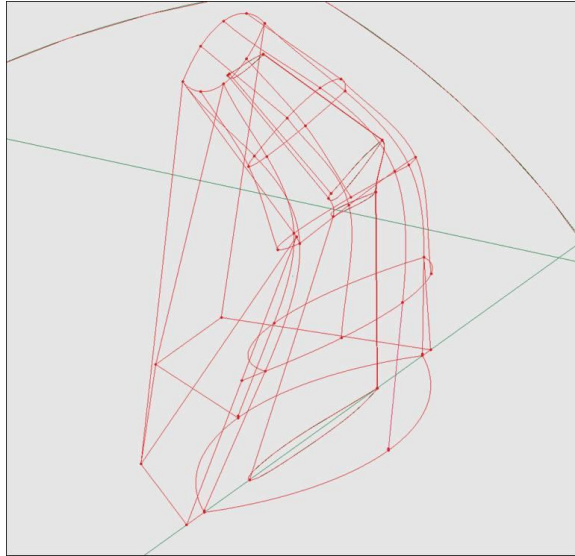


Figure 14 Elbow Section Connectors

The skeleton that establishes the size and location of the flat plate was built next, see Figure 15.

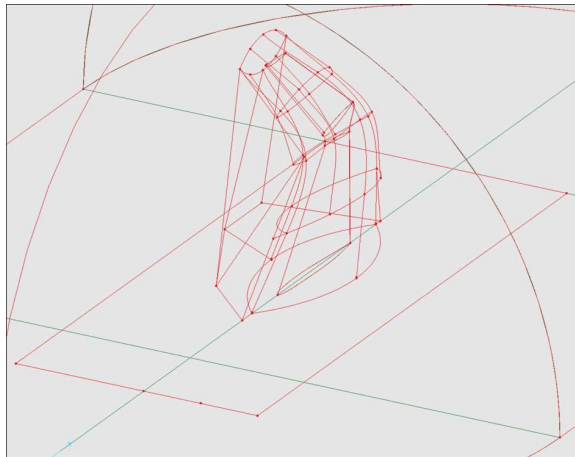


Figure 15 Flat Plate Connectors

Finally, the connectors that designate the position of the cells upstream of the wing were constructed. These connectors extend from the flat plate connectors to the sheath and elbow enclosure, see Figures 16.

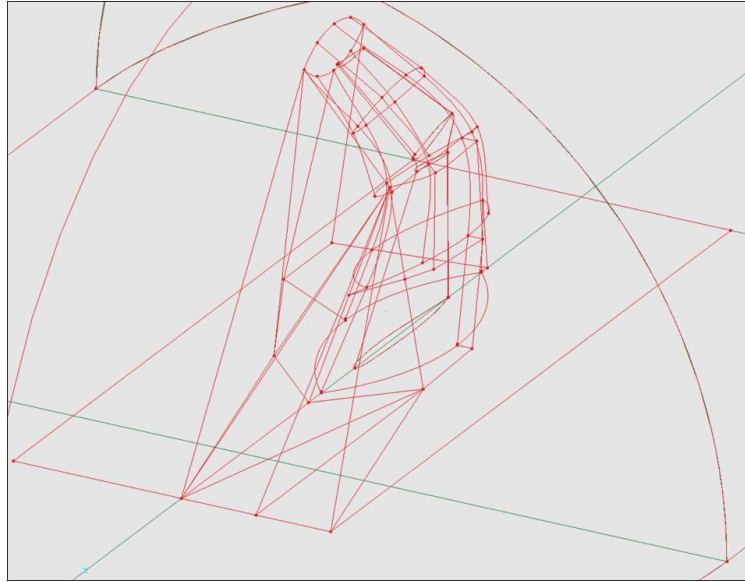


Figure 16 Upstream Connectors

3.2.4 Nodes. Once the connectors are in place, nodes could be placed and distributed. These nodes, or grid points, serve to divide the connectors into individual cell edges, thereby defining the cell size[18]. By placing more or less nodes on a connector, the number of cells surrounding that connector can be increased or decreased as necessary. Selection of the distribution of the nodes allows cells to vary in size along a single connector. For the connectors on the leading edge of the main wing and winglet a large number of nodes were added to ensure a fine meshing at the leading edge of the wing. Also on the trailing edge of both the main wing and winglet, nodes were placed sparsely at the main wing root and winglet tip, and crowded at the elbow, see Figure 17.

The nodes were concentrated toward the leading edge on the connectors at the root of the main wing and the tip of the winglet. Figure 18 shows the distribution of nodes on the wing root and winglet tip.

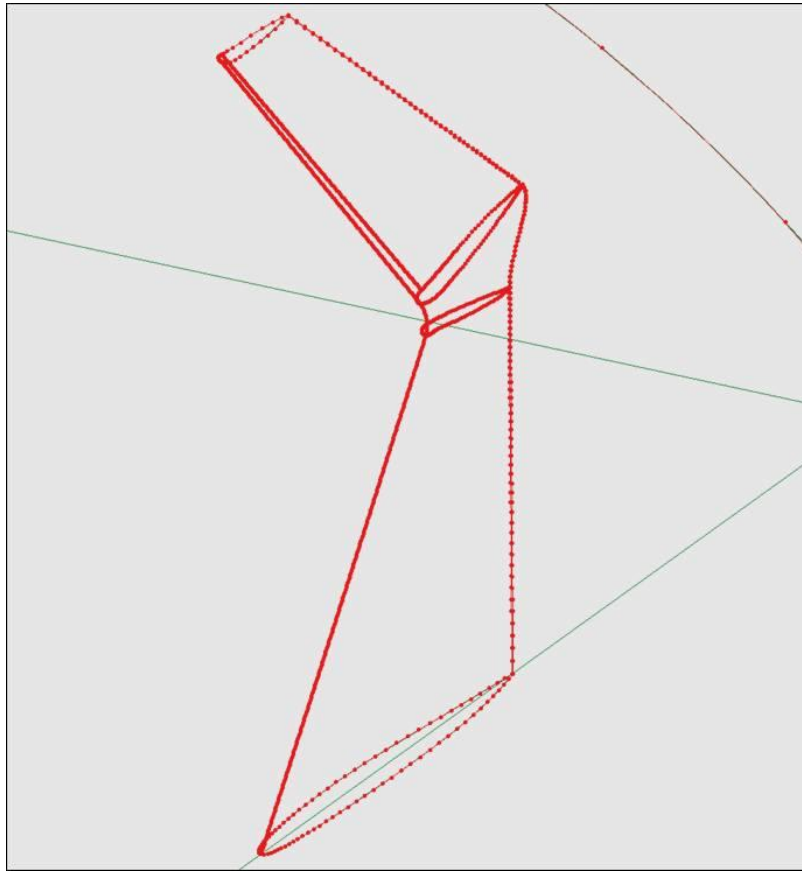


Figure 17 Nodes on the Leading and Trailing Edge Connectors

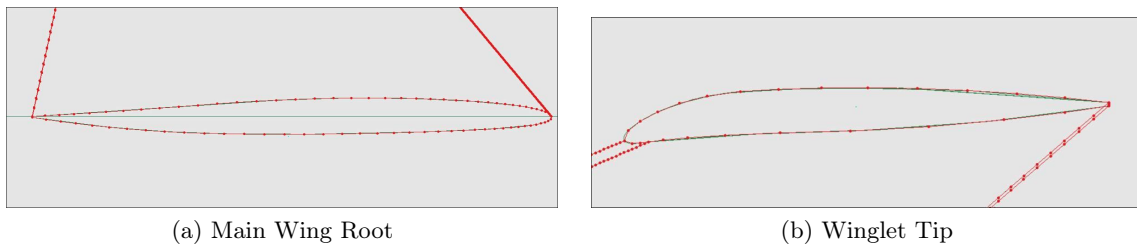


Figure 18 Nodes on the Main Wing Root and Winglet Tip

The nodes on the main wing tip and the winglet root, both at the elbow of the wing, also favor the leading edge. These connectors were given a high number of nodes to keep cell density high in the elbow region, see Figure 19.

The sheath, elbow enclosure and part of the upstream structure were all given nodes based on an average spacing between nodes, see Figure 20. This value was selected based on the node spacing on the wing, ensuring that all cells in these sections were sized to

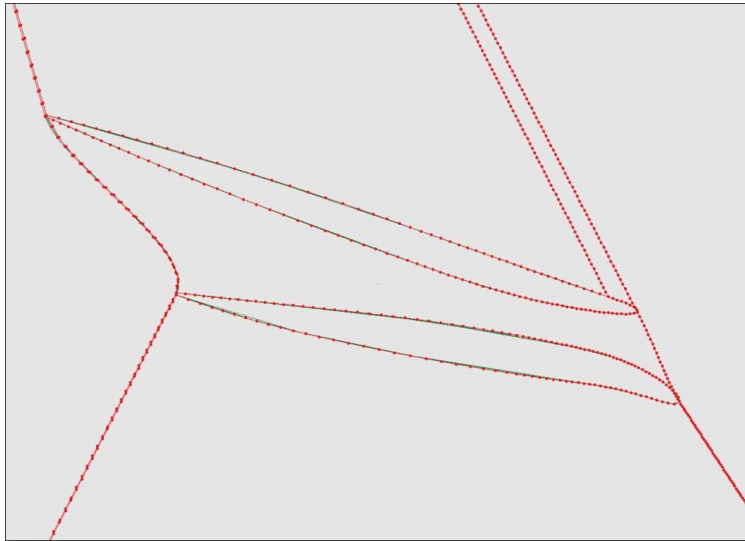


Figure 19 Nodes on the Elbow Connectors

guarantee a smooth transition between the cells on the surface of the wing and the cells in the surrounding area.

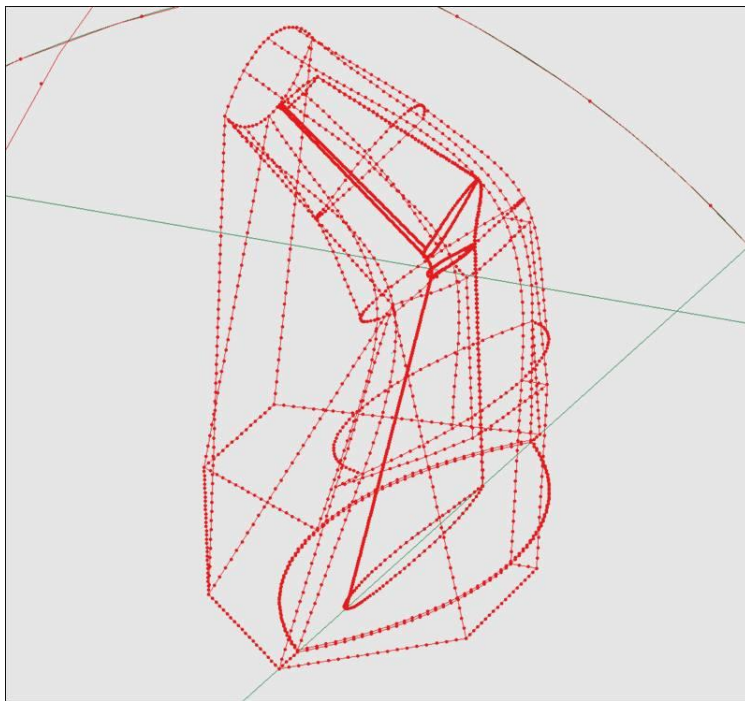


Figure 20 Nodes on the Sheath, Elbow, and Part of the Upstream Section Connectors

The flat plate was given a higher concentration of nodes in the sections upstream of the the wing. The nodes on the connectors that defined the area upstream of the wing were then placed to transition smoothly from the flat plate to the sheath and elbow enclosure, see Figure 21.

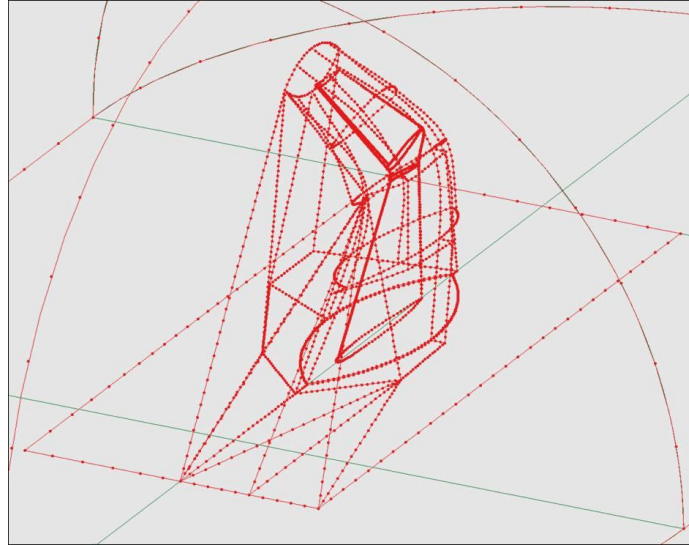


Figure 21 Nodes on the Upstream and Flat Plate Connectors

Finally the connectors composing the farfield boundary were given a fairly sparse distribution of nodes, see Figure 22.

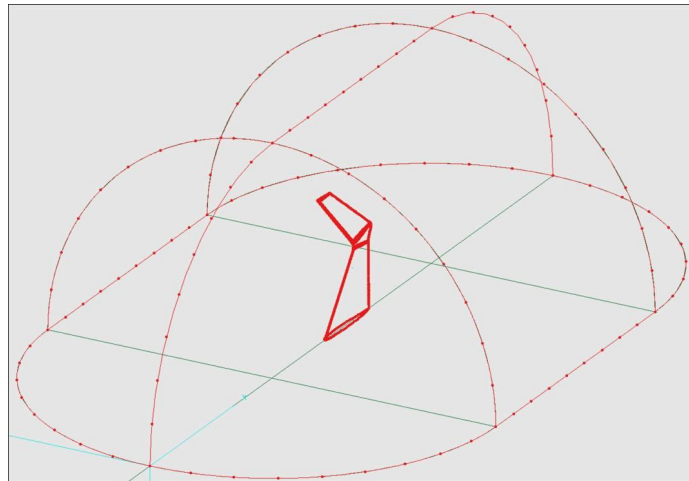


Figure 22 Nodes on the Farfield Connectors

3.2.5 *Domains.* Domains are Gridgen’s surface grids which define the number and arrangement of cells on a surface or plane within the grid. Domains are defined by a closed perimeter of connectors[18]. The first domains constructed were on the database defining the wing structure. By creating these domains using the ”On Database Entities” command the domains followed the contours and curvature of the wing database, which ensures that details of the wing are not lost due to the gridding process. In addition to creating the wing domains on the database the boundary decay factor was also adjusted to further manipulate the cell arrangement. The boundary decay factor controls the effect the boundary connector distribution has on the interior of the domain. A factor of 0 tells Gridgen that the interior cell size should not be affected by the boundary cell size and a factor of 1 ensures the cells on the domain interior do not exceed the size of the boundary cells. The default for this option is 0.5[18] . The top surface and the bottom surface of the main wing and winglet were both adjusted using a high boundary decay factor, which served to increase the number of cells at the leading edge of the wing, see Figure 23.

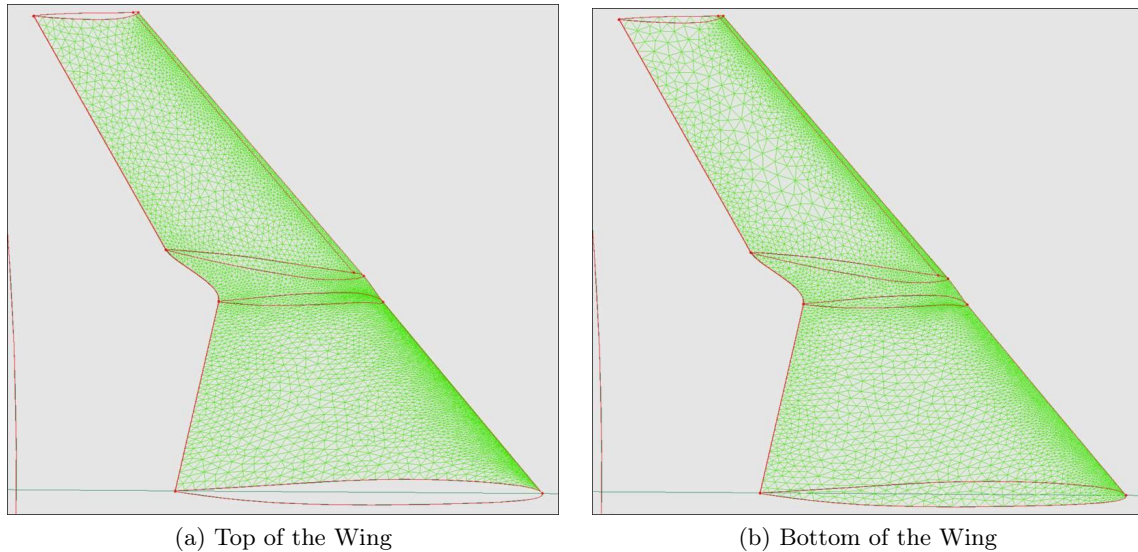


Figure 23 Domains on the Top and Bottom of the Wing

The domains on the sheath, elbow enclosure, upstream section, and flat plate were all created using a moderately high boundary decay factor, see Figure 24.

Finally the symmetry plane and farfield boundary domains were constructed using the default boundary decay factor, see Figure 25.

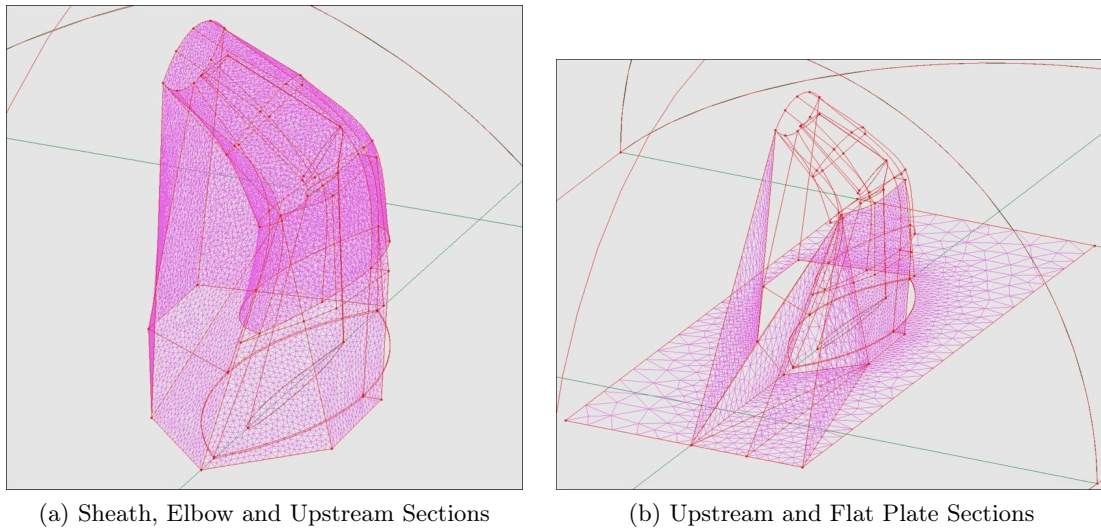


Figure 24 Domains on the Sheath, Elbow, Upstream and Flat Plate Sections of the Wing

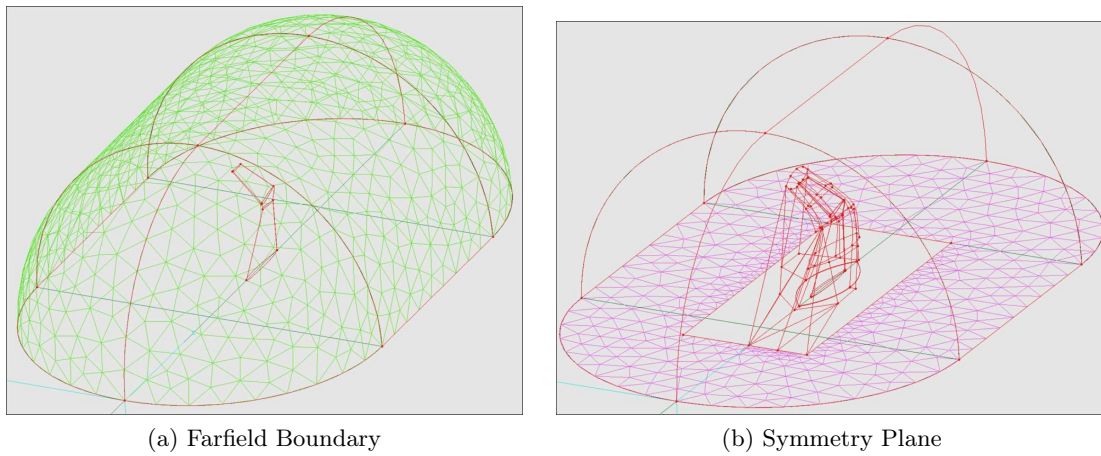


Figure 25 Domains on the Farfield and Symmetry Boundaries

3.2.6 *Blocks.* Blocks are 3D sections of the grid made up of a volume enclosed by a set of domains as the boundary[18]. The first block created was a prismatic block. This type of block consists of a user specified number of prismatic cell layers that are extruded from a domain[18]. The prismatic block was extruded from the portion of the flat plate directly surrounding the wing and the wing itself, see Figure 26. This prismatic layer will provide the mesh refinement necessary to solve the boundary layers that would grow on these surfaces. The block was created using 8 layers starting at a thickness of 0.01 and growing by 20%.

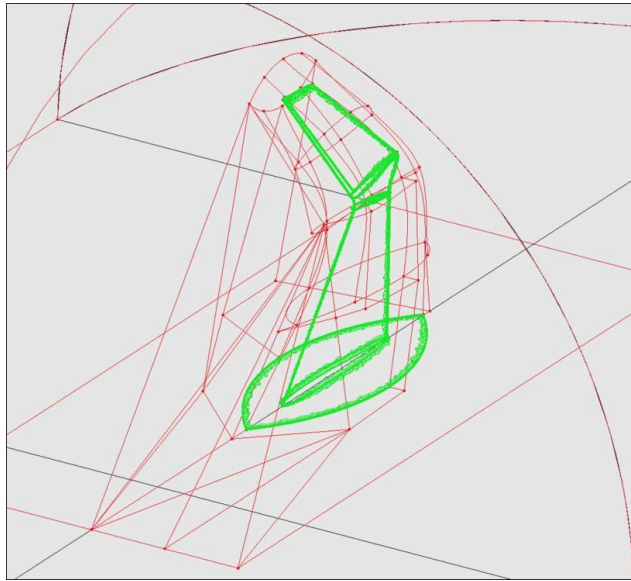


Figure 26 Prismatic Block

The sheath block was created next and utilized a moderately high boundary decay factor, see Figure 27.

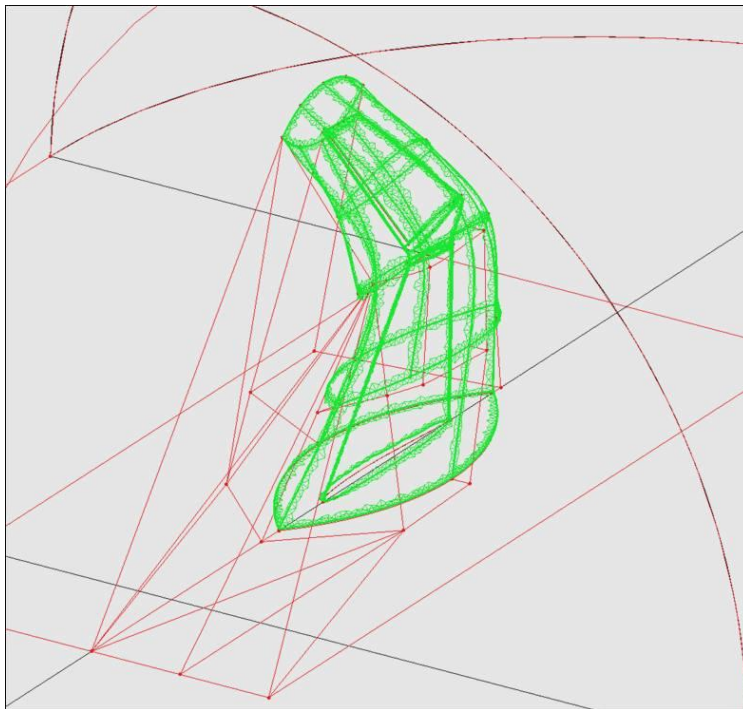


Figure 27 Sheath Block

The elbow enclosure blocks were then made and used an intermediate value for the boundary decay factor, see Figure 28.

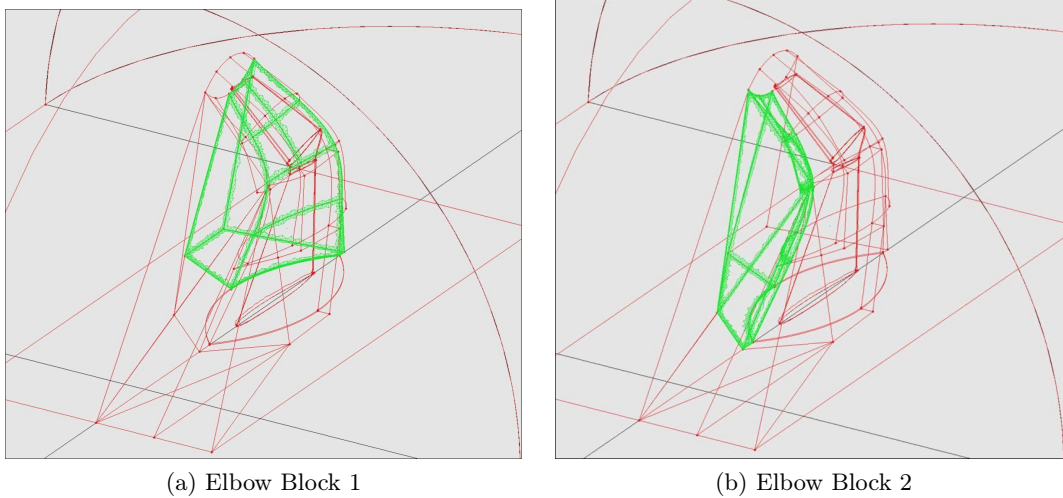
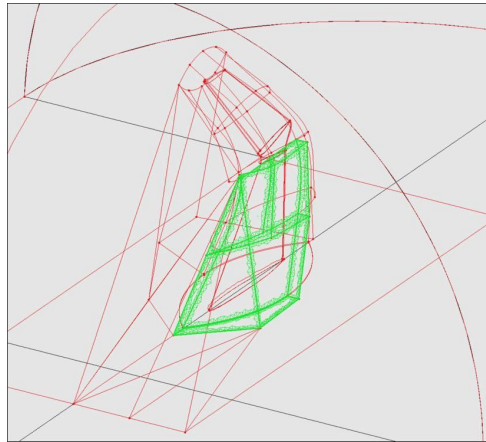


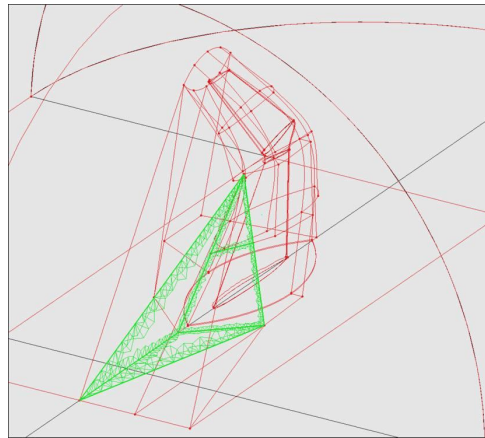
Figure 28 Elbow Enclosure Blocks

The upstream blocks were constructed next and a moderately high boundary decay factor was used, see Figure 29.

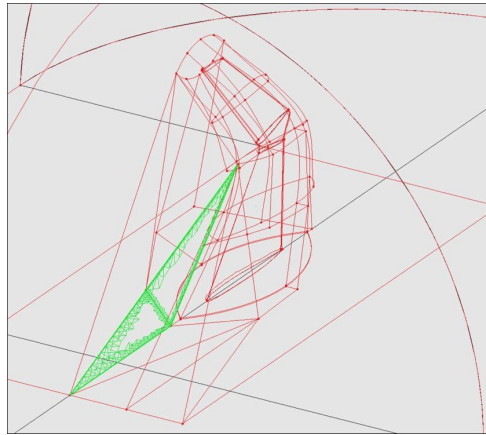
Lastly the block that filled the rest of the volume out to the farfield boundary was constructed. This block used a high boundary decay factor to ensure the transition from the structures directly surrounding the wing to the farfield boundary was smooth, see Figure 30.



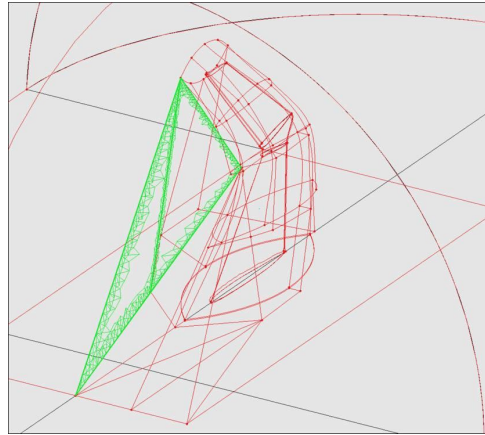
(a) Upstream Block 1



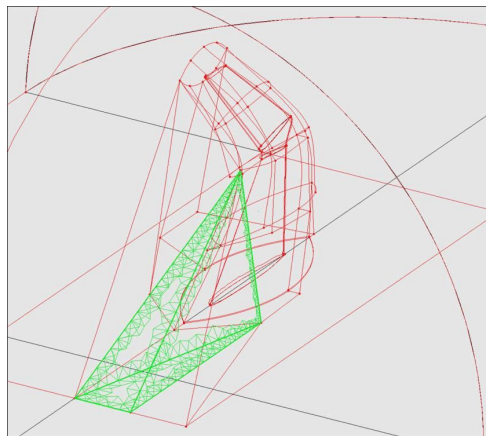
(b) Upstream Block 2



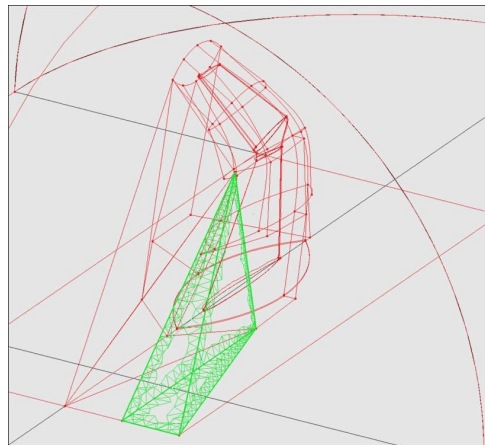
(c) Upstream Block 3



(d) Upstream Block 4



(e) Upstream Block 5



(f) Upstream Block 6

Figure 29 Upstream Blocks

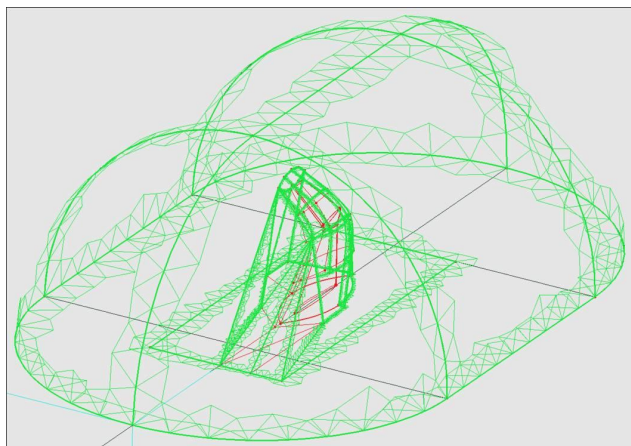


Figure 30 The Farfield Block

3.2.7 Boundary Conditions. To define the flow state at the boundaries of the grid a boundary condition file must be created. To generate this file first the surfaces that will define a particular condition are selected and given a condition number. For this research there will be four conditions. Once this is done the grid is opened using the Blacksmith utility provided with the AVUS code. In this utility each surface is given its flow conditions. The surface of the wing is given an "Adiabatic No Slip" solid wall boundary condition with force accounting. The adiabatic no slip condition specifies that the velocity is zero on the boundary, and that the normal pressure gradient and the normal density gradient are also zero. The no slip condition was validated by ensuring the values of Knudsen Number do not exceed 0.1 for the entire flight. By employing force accounting the code will calculate integrated forces and moments on the surface and output them. The second boundary is the flat plate, which is given the same boundary conditions as the wing surface minus force accounting. The third condition was a solid wall slip condition and was given to the symmetry plane surrounding the flat plate depicted in Figure 25b. The slip condition specifies flow tangency at the surface. The final condition is the farfield boundary condition which is defined as a "Modified-Riemann-Invariants". In this condition for supersonic cases all variables at inflow regions are held to user specified values and allowed to float at outflow locations. For subsonic cases Riemann Invariants are used at inflow positions and at outflow sections pressure is held at the user specified value and the other variables are allowed to float. The file, once created, is saved and will be called by AVUS when cases are run[19].

3.3 Flight Profile Data Point Selection

To determine the flight conditions to be used in simulations, the predicted flight profile of the rocket, provided by USAFA and shown in Figure 31, was used along with preliminary runs of the code. Appendix-A is a table containing the Mach number and altitude combinations chosen as data points to simulate along the flight profile as well as the range of angle of attack, α , for the tests. These data points range from Mach 0.5 at sea level to Mach 1.0 at 100 kft with a maximum Mach number of 4.5 occurring at 30 kft; this encapsulates both the acceleration and deceleration of the rocket as it gains altitude. A strong emphasis was placed on data points in the transonic region of the profile. Once these data points were selected the range of α was then chosen, where the zero angle of attack is referenced to the root chord of the main wing section. Initial simulations showed that at $\alpha = 0^\circ$ the C_l was negative, so 0° was chosen as the starting value of α . Initial results also showed that stall occurred above $\alpha = 15^\circ$ at sea level conditions, so 20° was selected to be the maximum value for α . Several values of α were chosen near the zero lift angle of attack, α_o , which is where the shock wave from the winglet has the largest effect on the lift of the wing.

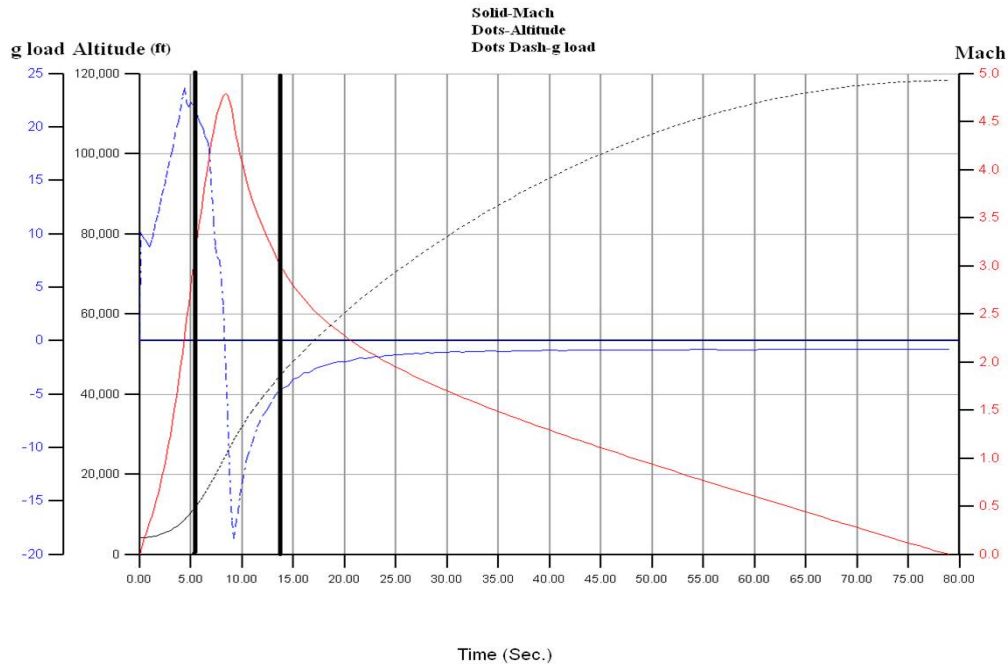


Figure 31 Predicted FLVIII Flight Profile

3.4 AVUS Code

The Air Vehicles Unstructured Solver, or AVUS, is a CFD code developed by AFRL/RB from research they conducted in the 1990s on unstructured grids. To run the code the user must provide the input files. The first file is the grid file, which was generated using Gridgen for this research as outlined in Section 3.2. The second is a boundary condition file, created using Gridgen and Blacksmith as outlined in Section 3.2.7. Finally a job file must be created, which performs the tasks outlined below[19].

3.4.1 Job File. The job file is used to submit cases to a cluster of processors which run AVUS; most importantly, it provides all inputs necessary for the code. The information in the job file initializes the runs by providing details such as file names and locations, the number of time steps in the simulation, and the number of processors to be used. Though this information is required for the simulations to run it will not be detailed here. A sample job file is attached in Appendix-B for reference on these parameters. The more important components such as the equation set and turbulence model used will be detailed in the following sections.

3.4.2 Navier-Stokes Equation Set. For this research the Navier-Stokes equations coupled with a turbulence model are used by the code to solve each case. The basic Navier-Stokes equations apply the conservation of mass, momentum, and energy equations to an arbitrary volume. This set of equations were chosen because they express the viscous forces as well as thermal conduction within the flow and avoid geometric and physical simplifications. Equation (1) shows the Navier-Stokes equations in integral form ignoring any source terms, where Ω is an arbitrary control volume, \vec{W} is the vector of conservative variables, and \vec{F}_c and \vec{F}_v are the vectors of convective and viscous fluxes respectively. A full description of the Navier-Stokes equations is provided in Appendix-C[20][21].

$$\frac{\partial}{\partial t} \int_{\Omega} \vec{W} d\Omega + \oint_S (\vec{F}_c - \vec{F}_v) dS = 0 \quad (1)$$

3.4.3 Spalart-Allmaras Turbulence Model. To model turbulence in the simulations the Spalart-Allmaras Turbulence Model was used. Turbulence models relate the turbulent

fluctuating correlations to the mean flow field quantities through addendum equations. This model is a one-equation model, meaning that there is one partial differential equation used in the model. In this one-equation model a partial differential equation is employed for the velocity component of the model whereas the component of length is specified algebraically. The Spalart-Allmaras model solves for a turbulent viscosity term, ν_t , which is then applied to the governing equation set, the Navier-Stokes equations by updating the flow viscosity. The governing equation of the Spalart-Allmaras model is given by Equation (2), and a complete set of equations for the model is provided in Appendix-D[22].

$$\begin{aligned} \frac{d\bar{\nu}}{dt} = \frac{3}{2} [\nabla \cdot ((\nu + \bar{\nu})\nabla\bar{\nu}) + 0.622(\nabla\bar{\nu})^2] + 0.1355\bar{S}\bar{\nu}(1 - f_{t2}) \\ - [3.239f_w - 0.806f_{t2} \left[\frac{\bar{\nu}}{d}\right]^2 + f_{t1}(\nabla q)^2] \end{aligned} \quad (2)$$

3.4.4 Gottlieb and Groth Riemann Solver. This algorithm is used to solve the Riemann Problem, which arises in determining wave and flow properties in regions divided by a contact surface. The solver selected for use in the code was developed by J. J. Gottlieb and C. P. T. Groth. In this solver the states at the grid nodes are defined by P , u , γ , R , and the speed of sound, a , rather than ρ . Gottlieb and Groth decided to use a instead of ρ because they found numerical computations were more efficient as a appears more frequently than ρ . Also instead of solving for the common pressure, P^* , as is done in most solvers, the common flow velocity, u^* , is found in this solver to again improve the computational performance. The fundamental equation used to solve for u^* is given in Equation (3) where l and r represent properties to the left and right of the contact and the prime denotes differentiation with respect to u^* . Appendix-E has a more complete outline of the procedure for the solver[23].

$$u_{i+1}^* = u_i^* - \frac{P_l^*(u_i^*) - P_r^*(u_i^*)}{P_l^{*'}(u_i^*) - P_r^{*'}(u_i^*)} \quad (3)$$

3.5 Grid Independence Check

Once the parameters for the AVUS code were finalized a grid independence study could be completed. A grid independence study is performed to ensure that the grid itself does not affect the simulation solution. To perform this study the first grid created was modified by increasing the number of nodes on the connectors to roughly double the overall number of cells in the volume. Next both of these grids were used to run simulations on 9 of the flight condition cases outlined in Appendix-B. The C_l and C_d results for these cases were plotted against Mach number and compared to see if there was a difference between the solutions obtained from each grid. The outcome of this initial test showed independence for some cases, but not all. So, a third grid was created in the same manner as outlined above again doubling the number of cells from the previous grid and the same 9 cases were run. These results are not as decisive as was desired, however, after consideration a completely grid independent solution would be nearly impossible to obtain with a single grid considering the amount and variety of simulations being run. The error bars in Figure 32 depict $\pm 5\%$ from the average of the coefficients. As seen in the figure, the first grid which was to be used for data collection fell within 5% for all 9 cases. This confirms the grid will have virtually no effect on the results of the simulations.

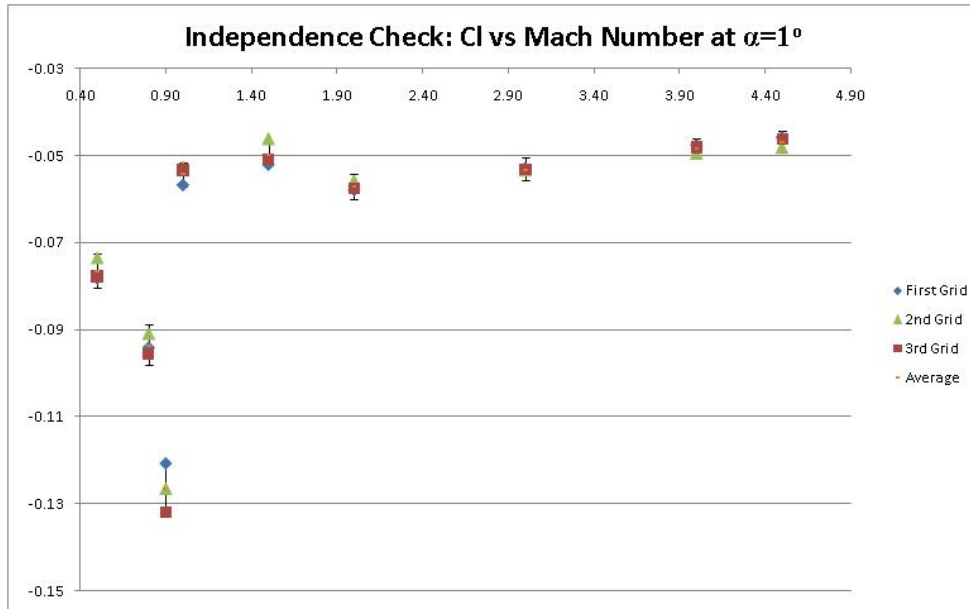


Figure 32 Grid Independence Check

3.6 Finite Element Analysis

Another concern of the grid affecting the CFD solution is the amount the actual wing will deflect during flight, changing the lifting characteristics of the wing. While the CFD grid cannot replicate the wing deflections, a finite element analysis of the wing was conducted by 2Lt Michael Vinacco to estimate the total deflections of the wing throughout the flight profile. Lt Vinacco was given the pressure distribution over the surface of the wing for 5 separate cases within the flight profile. These cases were Mach 1 at 5 kft and 100 kft, Mach 2.5 at 9 kft and 60 kft and Mach 4.5 at 30 kft. The pressures from these cases were distributed over his finite element model of the wing then the static deflections were calculated. Through this analysis it was found that the maximum deflections of the wing were on the order of 0.6 inches at the tip of the winglet. This amount of deflection is small enough that the lifting characteristics of the wing will not change enough for wing deflection to be a concern in the CFD simulations presented here[24] .

3.7 Convergence Tests

To ensure the test cases converge to a steady state solution, the finite difference derivative of density was plotted. The solution was considered converged if the plot asymptotically converged on a number much less than one before the maximum number of iterations are reached. If a solution did not reach convergence it was re-simulated with an increased number of iterations and checked again for convergence. Figure 33 shows a typical plot obtained from a converged solution.

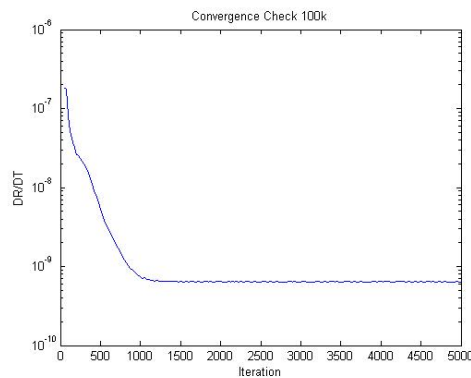


Figure 33 Typical Convergence Plot

IV. Results

The results obtain from the CFD analysis of the experimental wing and winglet geometry are presented in the sections below. These results show the lift and drag coefficients, normalized by the planform area of the main wing section (416.13cm^2), plotted against Mach number and α . A detailed description of the winglet shock wave and its effect on the main wing lifting characteristics is also provided. Additionally, temperature data due to the shock interactions in the elbow of the wing is also presented. Finally it explains the reasoning for the recommendation to mount the wing at a 3° angle of attack on the rocket.

4.1 Lift and Drag Characteristics

One of the first pieces of information to gather from the data was the angle of attack corresponding to zero lift and minimum drag. To accomplish this, values of C_l and C_d were plotted against α upon completing the simulations and ensuring convergence. Figures 34 and 35 show C_l and C_d plotted for values of Reynolds Number ranging from 5.6×10^4 to 8.8×10^6 . From these plots it is apparent that the α value for zero lift and minimum drag are between 2° and 6° depending on Mach number.

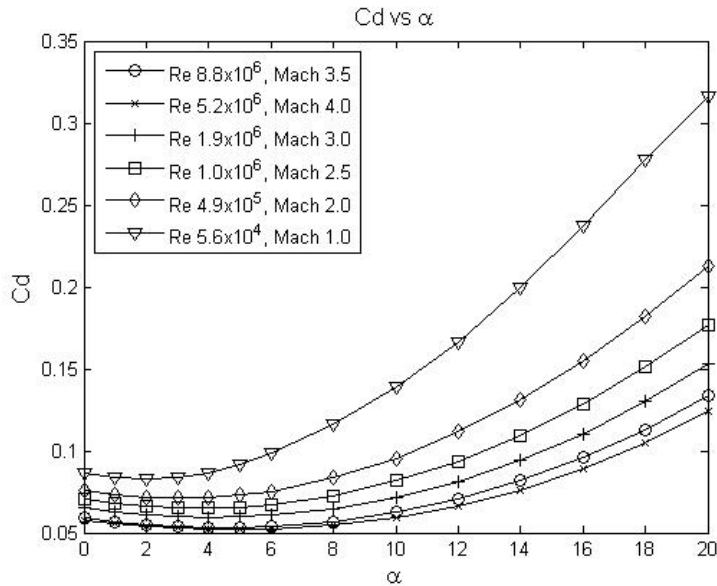


Figure 34 C_l Against α for a Range of Reynolds Numbers

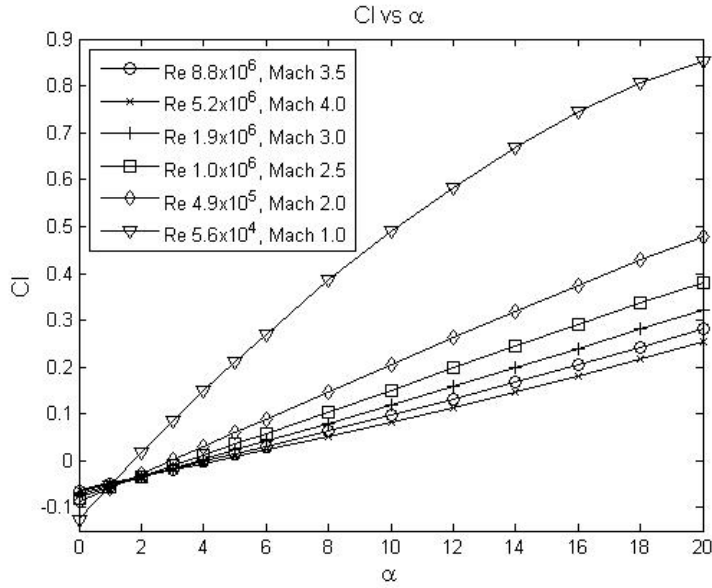


Figure 35 C_d Against α for a Range of Reynolds Numbers

It is of considerable importance that C_l and C_d are accurately predicted for the entire flight profile, especially from about Mach 2 to 4.5 which is the high speed region of the flight. These Figures both show that the coefficients become more constant with increasing Reynolds Number, which is encouraging for flight prediction in the high speed region of the experiment. This means at higher Reynolds Numbers, above Mach 2, the values of C_l and C_d remain fairly constant for a given angle of attack and a single value of C_l and C_d can be used confidently in flight predictions. To show this more clearly the lift curve slope, $C_{l\alpha}$, which describes the change in lift coefficient per degree angle of attack, was plotted against Mach number, see Figure 36. This plot shows that the change in lift coefficient is relatively constant throughout the high speed portion of the flight. For comparison, Figure 37 is another $C_{l\alpha}$ plot for flight test data from the X-15 Research Aircraft presented in John J. Bertin's *Hypersonic Aerothermodynamics*. One can easily see that the trends seen in the simulations match the same trends obtained from X-15 test data[6].

For further verification of the data collected in the simulations, maximum lift to drag ratio, $\frac{L}{D_{max}}$, was plotted against Mach number, see Figure 38. In this plot it was expected that $\frac{L}{D_{max}}$ would become constant as Mach number increased based on the Mach number independence principle. The Mach number independence principle states that at

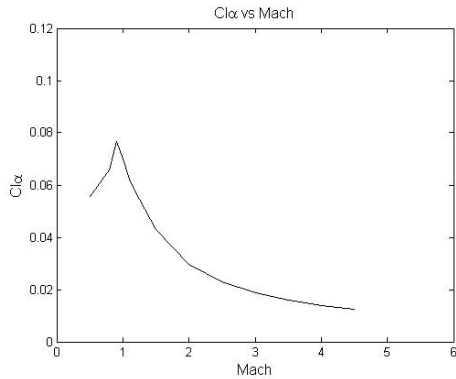


Figure 36 $C_{l\alpha}$ vs Mach Number, Simulations

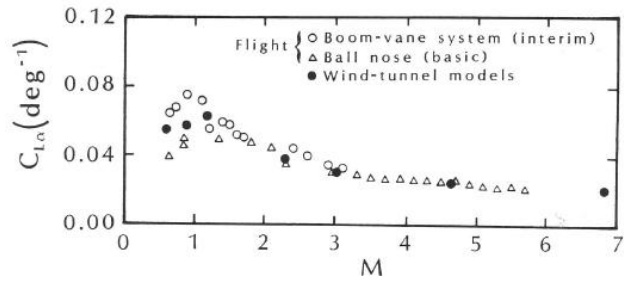


Figure 37 $C_{l\alpha}$ vs Mach Number, Bertin [6]

high Mach numbers certain aerodynamic quantities such as lift coefficient and wave drag coefficient become essentially independent of Mach number. Figure 38 is the data obtained in simulations and Figure 39 is X-15 test data. Again the simulated plot for $\frac{L}{D_{max}}$ does indeed become constant at higher Mach numbers corresponding to the X-15 flight test data. The trends in the $C_{l\alpha}$ and $\frac{L}{D_{max}}$ plots provide evidence that the data collected in simulation matches theoretical and experimental expectations[6][25].

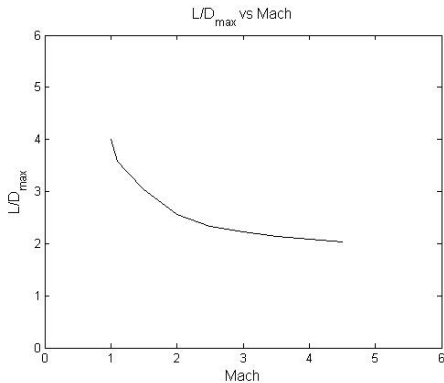


Figure 38 $\frac{L}{D_{max}}$ vs Mach Number, Simulations

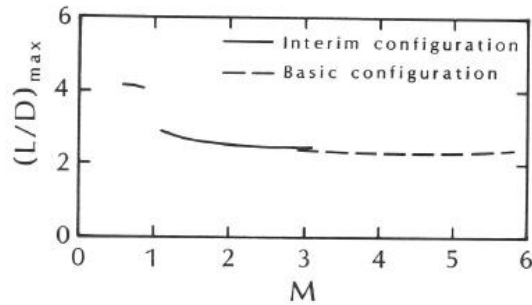


Figure 39 $\frac{L}{D_{max}}$ vs Mach Number, Bertin [6]

4.1.1 Lift Characteristics. Once the simulations were completed and convergence was verified, the values of C_l were then plotted against Mach number and α . With α values of 0° and 1° there is a relatively constant coefficient for the supersonic region as seen in Figures 40 and 41. However, there is noticeable decrease in lift for this wing at higher angles

of attack in the supersonic region. This drop becomes evident starting at $\alpha = 2^\circ$, as seen in Figure 42. At 2° the overall lift of the wing remains negative for a majority of the the flight profile, only becoming positive in the transonic region. At 3° and the lift is positive for the first half of the flight and is driven negative in the supersonic region of the flight, as seen in Figure 43. Figures 44 and 45 show C_l plotted against Mach number at α values of 4 and 5 degrees. In these cases the lift is positive and drops to zero at high Mach numbers. At 6° C_l the decrease in lift is present, but lift remains positive throughout the flight profile, see Figure 46. The trends seen at 6° continue throughout all other angles of attack and are included in Appendix F. This decrease is consistent with Figures 36 and 37 where an increase in Mach is paired with a decrease in C_l .

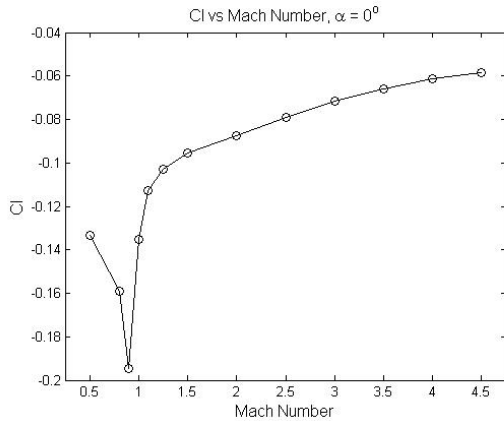


Figure 40 C_l vs Mach Number $\alpha = 0^\circ$

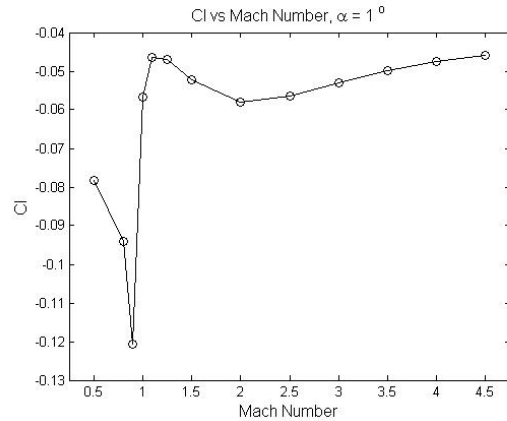


Figure 41 C_l vs Mach Number $\alpha = 1^\circ$

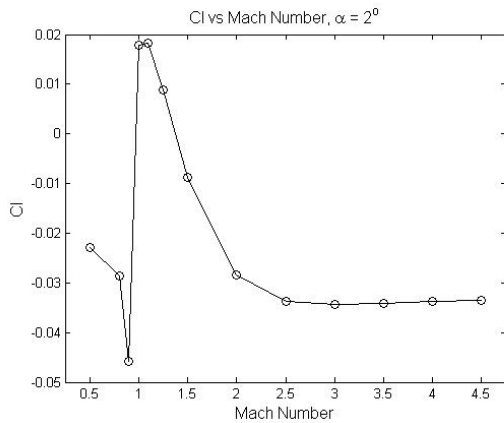


Figure 42 C_l vs Mach Number $\alpha = 2^\circ$

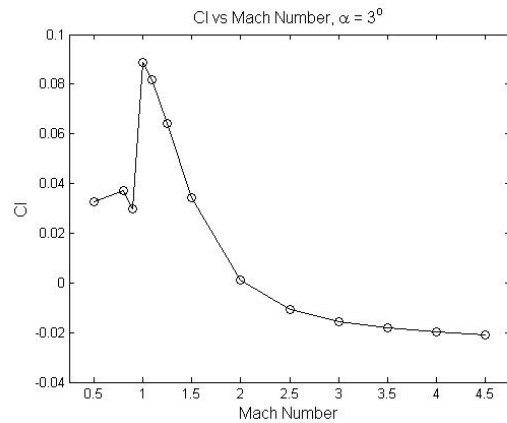


Figure 43 C_l vs Mach Number $\alpha = 3^\circ$

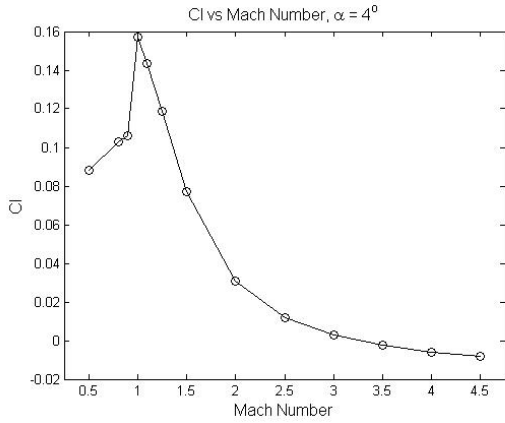


Figure 44 C_l vs Mach Number $\alpha = 4^\circ$

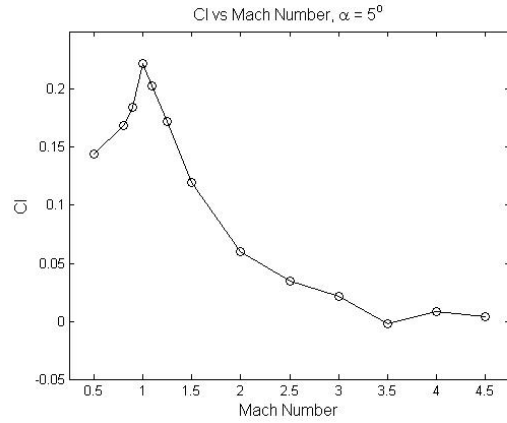


Figure 45 C_l vs Mach Number $\alpha = 5^\circ$

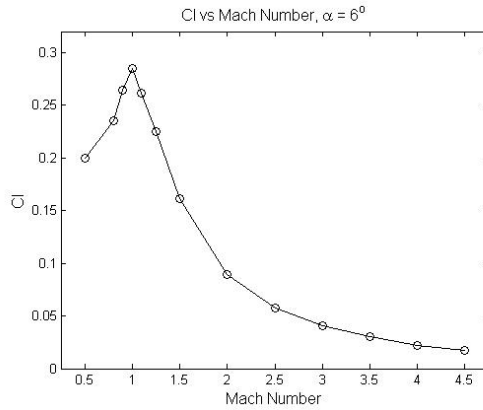


Figure 46 C_l vs Mach Number $\alpha = 6^\circ$

Though this decrease in lift coefficient with increasing Mach number is consistent with theory, it was important to find the cause to rule out error in the simulations. Further inspection revealed the cause was the interaction of the winglet shock wave with the main wing. It is important to note here that the main wing has both aerodynamic and geometric twist. Therefore the angle of attack at the main wing tip just before the winglet is less than that of the root and subsequently produces less lift. Once the wing has entered the supersonic region a shock wave forms on the winglet. Figure 47 shows the development of the shock wave on the surface of the main wing from Mach 1.1 to 4.5 at 2° angle of attack. This shock wave forms in the elbow region of the wing and impinges on the upper surface of the main wing section where the angle of attack is already reduced by the physical geometry. The pressure on the main wing is increased where the shock wave forms; this

causes a decrease in the pressure difference between the top and bottom surfaces of the wing from shock location to the wing tip. The increased pressure on the upper surface causes a loss of lift at the tip of the main wing section. The final result is the overall lift of the wing is dependent on the strength of the winglet shock wave.

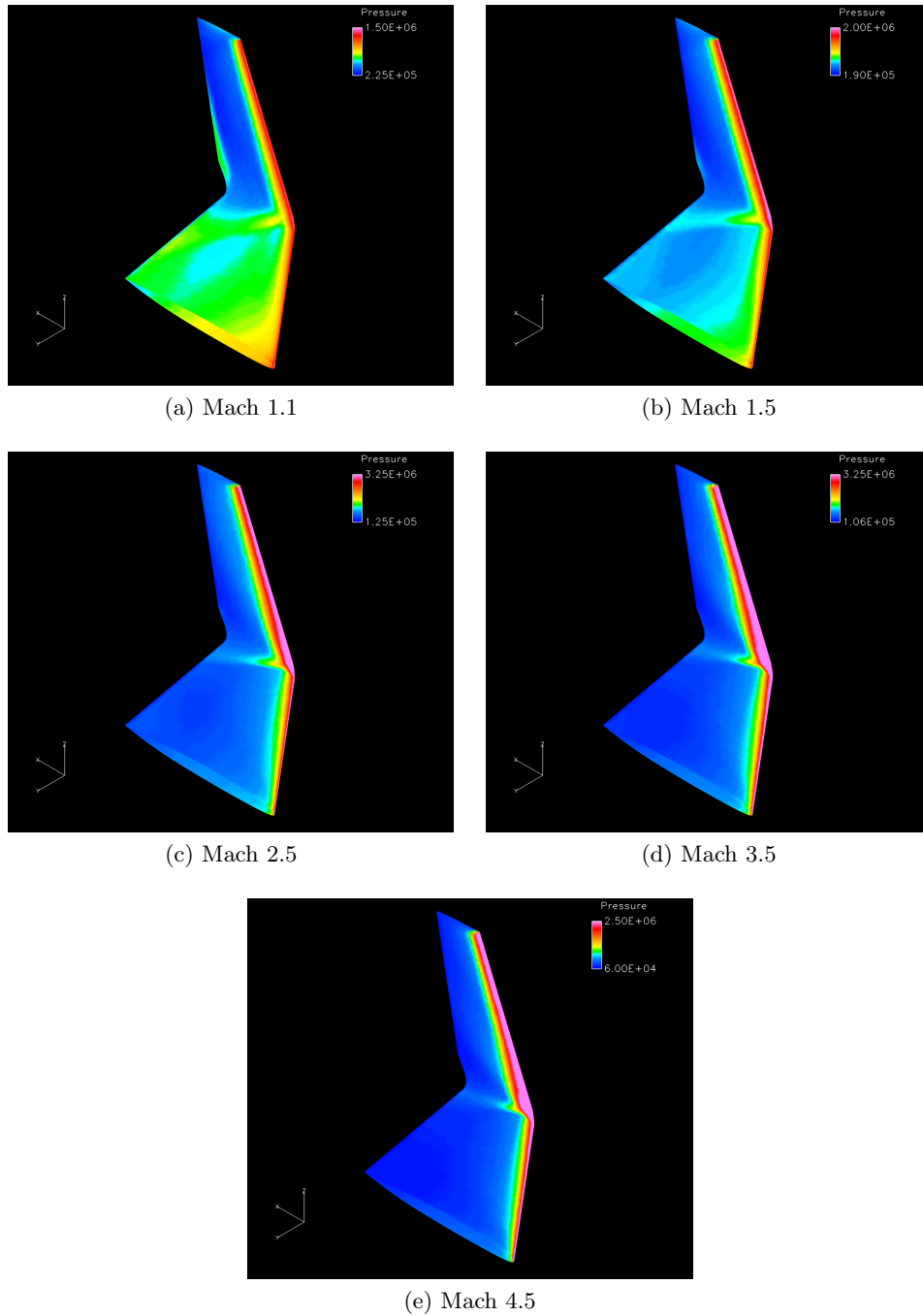


Figure 47 Winglet Shock Wave Development

As the winglet shock wave forms, it impinges on a large angle and covers a large portion of the main wing span as seen in Figure 47a. Though the area affected is great, the pressure increase due to this weak shock wave is small and lift remains relatively high. As speed increases the impingement area of this shock wave on the wing decreases, therefore less and less of the main wing surface is affected. Though the area influenced by the shock is decreasing, the strength of the shock grows, causing a more significant reduction in the lift generated in the effected area. Surface pressure contours of the top and bottom surface of the wing are presented in Figure 48 for the 2° , Mach 2.0 case. The contours were taken from the Mach 2.0 case because at this speed the effects from the shock wave are well developed. In these figures one can see that the upper surface has lower pressures than the lower surface in all locations except in the location of the winglet shock wave. In the area effected by the shock wave the pressures on the upper and lower surfaces are nearly equal and at some points the pressure on the upper surface is higher. This causes the area to produce slightly negative lift, reducing overall lift. Figure 49 shows the upper and lower surface pressure contours for the 2° Mach 3.5 case. In these figures pressures on the top and bottom surface of the wing have lowered from the Mach 2.0 case. Because the overall pressure of the wing is reduced the lift generated is reduced and the pressure rise due to the shock wave is more effective.

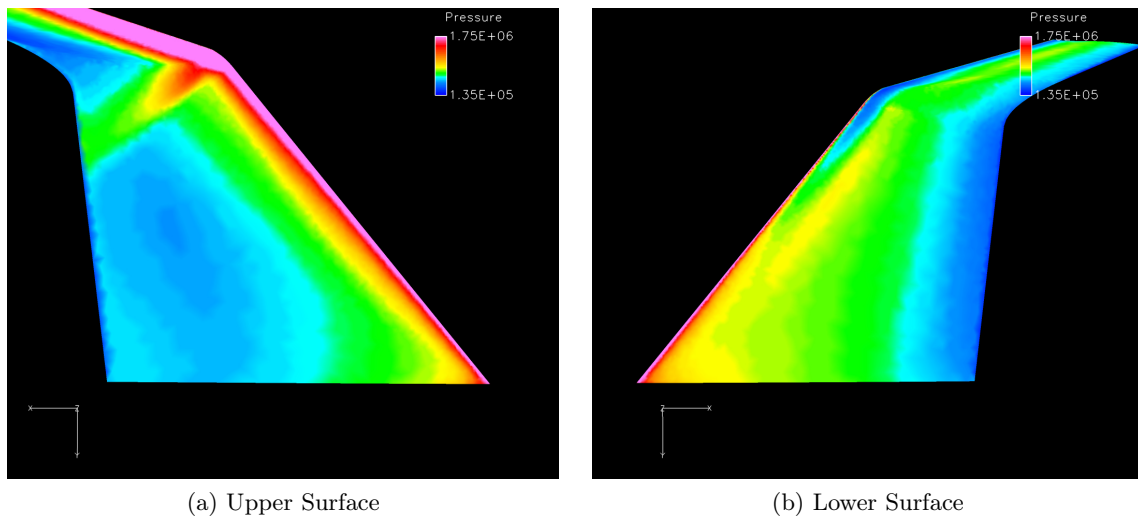


Figure 48 Pressure Distribution of Upper and Lower Surfaces at Mach 2.0 and 2°

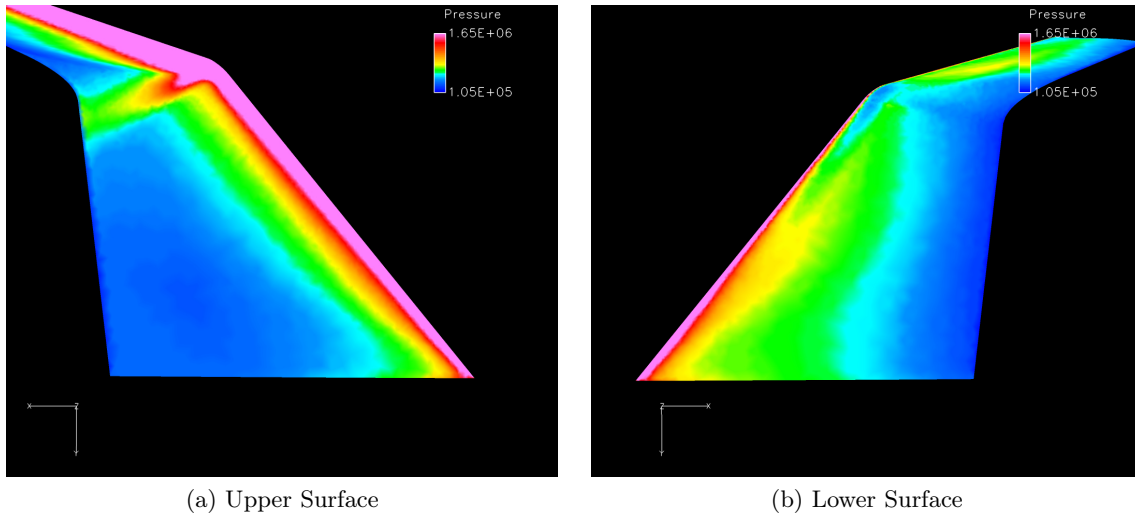


Figure 49 Pressure Distribution of Upper and Lower Surfaces at Mach 3.5 and 2°

To further visualize the shock wave as it forms on the wing, chordwise pressure contour planes are shown in Figure 50. Figure 50f shows the locations of the chordwise pressure contour planes. The plane closest to the root, Figure 50a, there is no variations in pressure except those resulting from the shock wave forming from the leading edge of the main wing. Figure 50b is at roughly half the span of the wing and a high pressure region becomes evident above the wing highlighted by an arrow. Moving toward the elbow of the wing in Figure 50c the high pressure region above the wing has moved to the surface of the wing and it begins to match the location of the high pressure region on the surface of the wing marked with arrows. The wave continues to follow the high pressure region on the surface of the wing and grow in strength getting closer to the elbow in Figures 50c, 50d and 50e respectively.

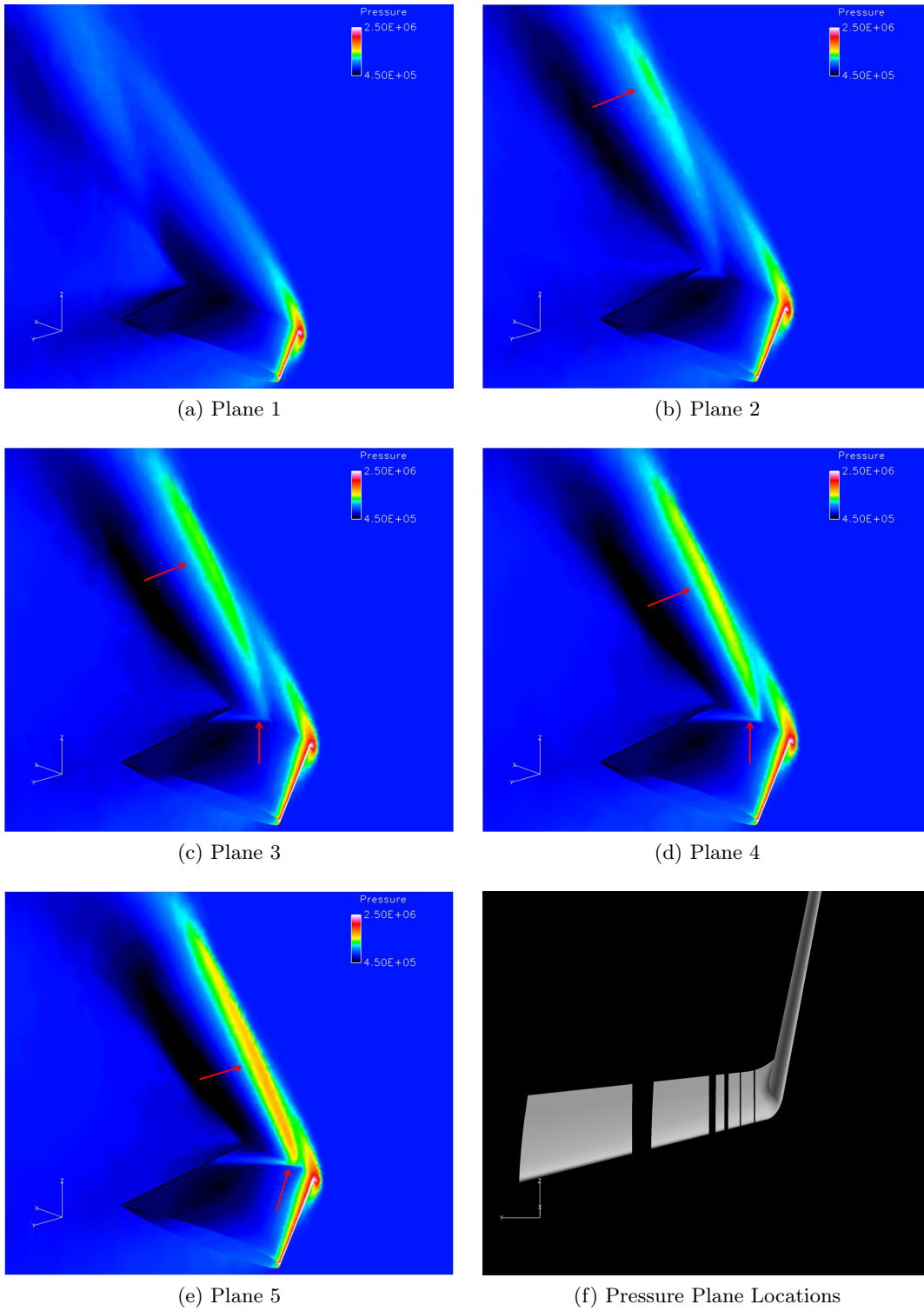


Figure 50 Chordwise Pressure Contour Planes

Overall it is clear that the winglet shock wave does decrease the overall lift of the wing. The shock wave brings down the overall lift around Mach 2.0 because it causes the lift near the winglet to be slightly negative. As Mach number increases, even though the winglet shock wave is effecting less and less of the wing, the lift generated by the main wing is decreasing keeping the lift low. Overall, the decrease in lift is significant enough to affect flight stability and therefore should be addressed in the experiment.

4.1.2 Drag Characteristics. In addition to the coefficient of lift, the coefficient of drag was also plotted against Mach number. Figure 51 shows the coefficient of drag at an α of 2° performing in the manner expected. Approaching the transonic region there is a rise in C_d , followed by a steady decrease once the flow over the wing is entirely supersonic reflecting the decrease in $C_{l\alpha}$ and the total zero lift drag as in the X-15. Because there were no obvious abnormalities in the drag profile and the C_d values obtained in simulation matched trends seen in the X-15, there was not a significant focus placed on an analysis of the drag profile. Plots for all other angles of attack are in Appendix G.

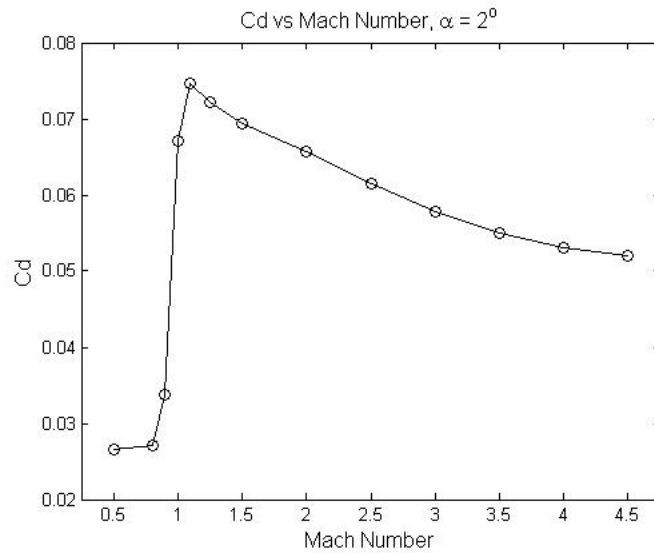


Figure 51 C_d Against Mach Number at $\alpha = 2^\circ$

4.2 Shock-Shock Interactions and Temperature Distribution

The next major component of this study was to investigate the temperature distribution over the wing, which was expected to be heavily influenced by shock-shock interactions. The temperature distribution on the surface of the wing for an angle of attack of 2° and Mach 4.5 was examined; this yielded a maximum temperature of 1180 Kelvin. This maximum temperature is consistent with a stagnation temperature, where the predicted stagnation temperature is 1155. Figures 52a and 52b show the temperature distribution on the upper and lower surfaces for this case. The maximum temperature is at the stagnation point on the leading edge near the root of the wing (see Figure 52c). There is also a temperature increase in the region of the winglet shock wave on the upper surface of the wing.

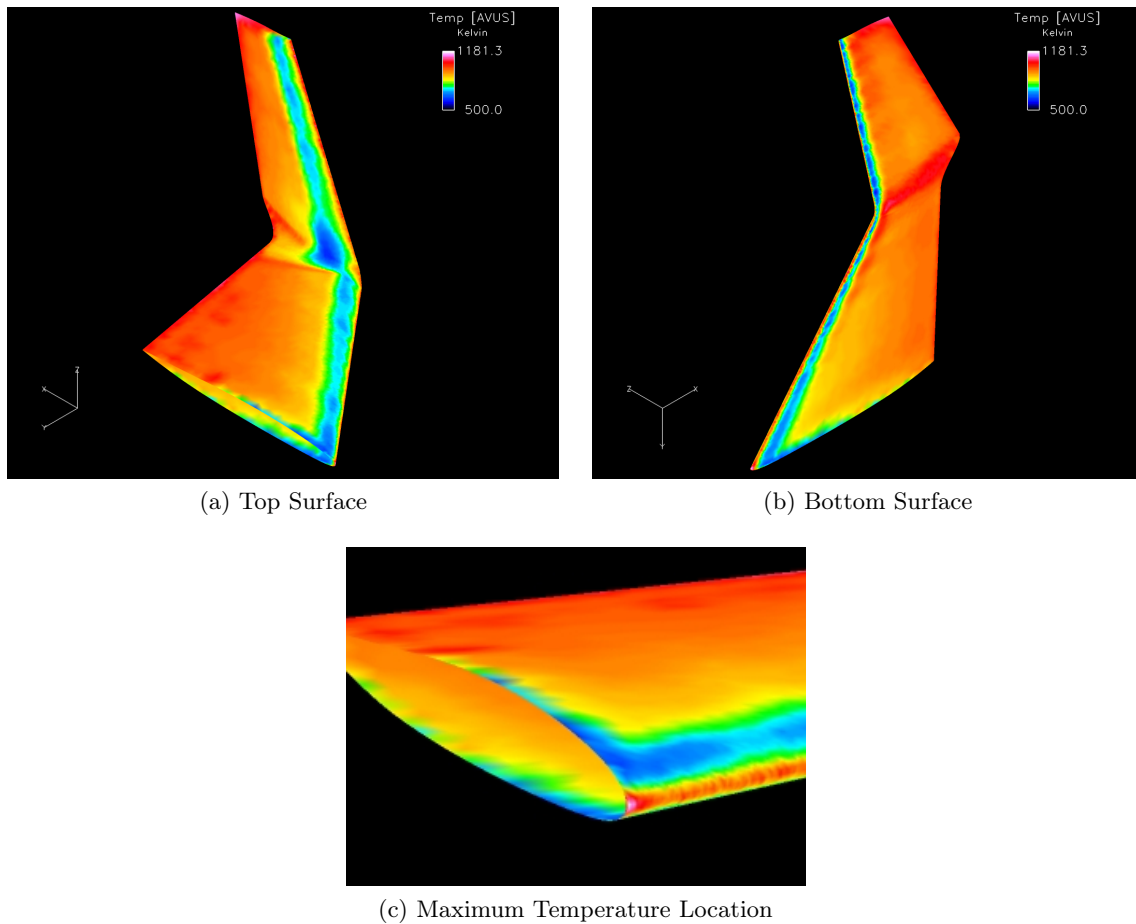


Figure 52 Temperature Distribution at $\alpha = 2^\circ$

To further investigate the shock wave interactions temperature contours were created in planes cut through the wing. Figure 53e shows the locations of the planes on the wing. The planes are presented in Figure 53 and represent locations on the wing from the quarter chord in 53a to the mid-chord in 53d. In the first plane, Figure 53a, the shock waves from the main wing and winglet are visible. Upon closer inspection of the intersection point between the two shock waves, circled in the figure, a slight temperature rise, on the order of 200 degrees, near the winglet is evident. This temperature increase is caused by the interactions between the shock waves formed by both the main wing and winglet. The interactions on this wing can be classified as hybrids between the Type-V and Type-VI interactions as outlined in John D. Anderson's *Hypersonic and High-Temperature Gas Dynamics*. These types of interactions involve two shock waves moving in the same direction, intersecting each other at a point where flow is supersonic upstream and downstream of the waves[25]. Also in this plane there is a spike in temperature where the winglet shock wave impinges on the main wing, highlighted by an arrow. In the second plane, Figure 53b, the increased temperature area due to the shock-shock interaction becomes larger and more defined, but decreases in temperature. The winglet shock wave impinging on the main wing also decreases in temperature and begins to move away from the winglet. In Figure 53c the location of the shock-shock interaction begins to move away from the surface of the winglet. The final plane, Figure 53d, shows a complete separation of the interaction point from the wing surface and a significant weakening of the winglet shock wave formed on the main wing. The separation makes sense because the shock waves are farther and farther removed from the surface of the wing as they progress downstream, causing their intersection point to also remove itself from the surface of the wing.

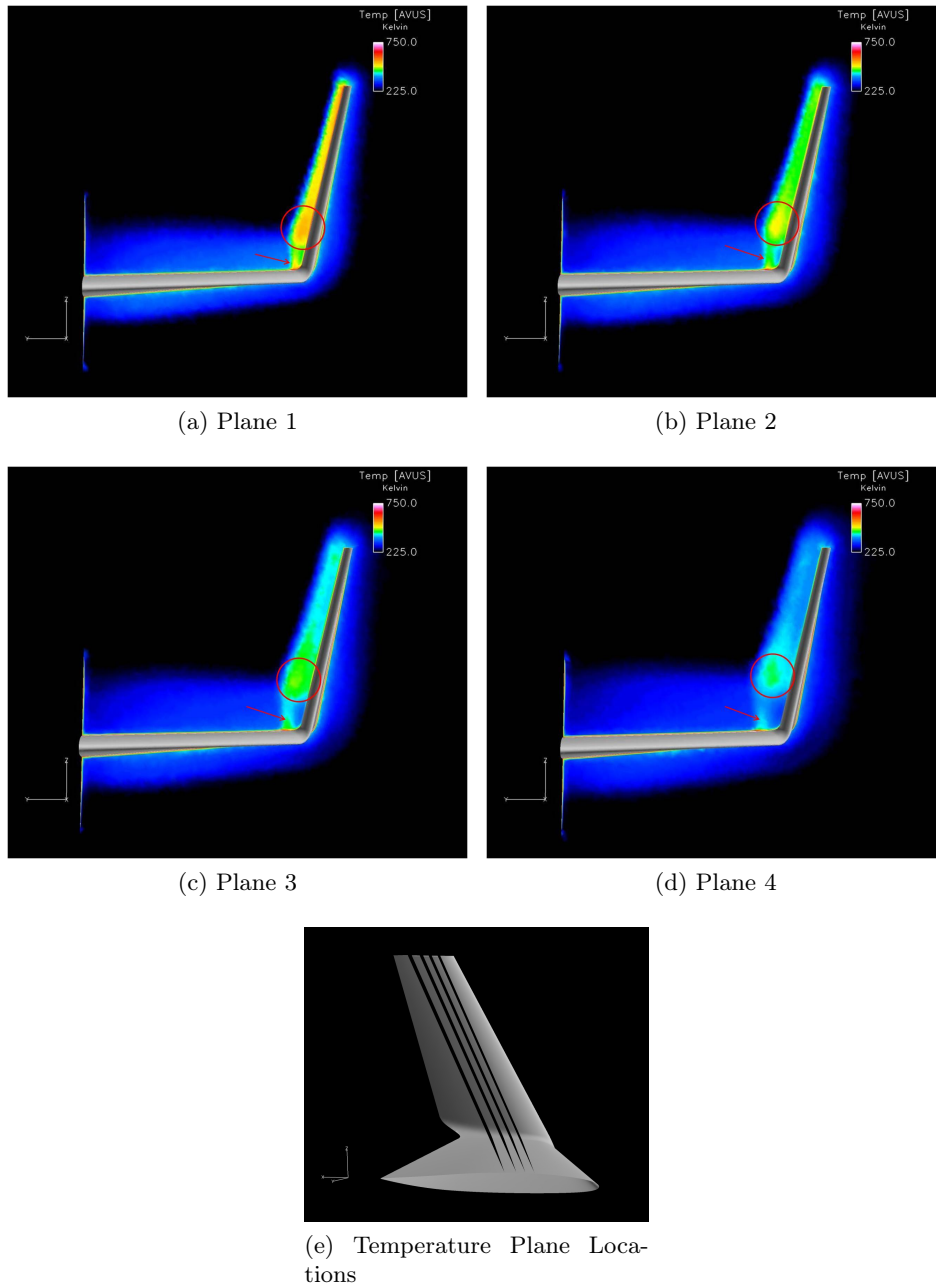


Figure 53 Temperature Contour Planes, 2° , Mach 4.5

For the effect of the shock-shock interactions on the wing temperature distribution to become clear, the temperature contour planes in Figure 53e are shown with surface temperature contours, see Figure 54. With both contours presented on the same scale it is apparent that the interactions between the shock waves do not have an effect on the surface temperatures because the surface temperatures are much larger than the temperatures

created by the shock-shock interactions. However, the location of the winglet shock wave on the surface of the main wing lines up directly with an increase in temperature on the surface and is highlighted by an arrow.

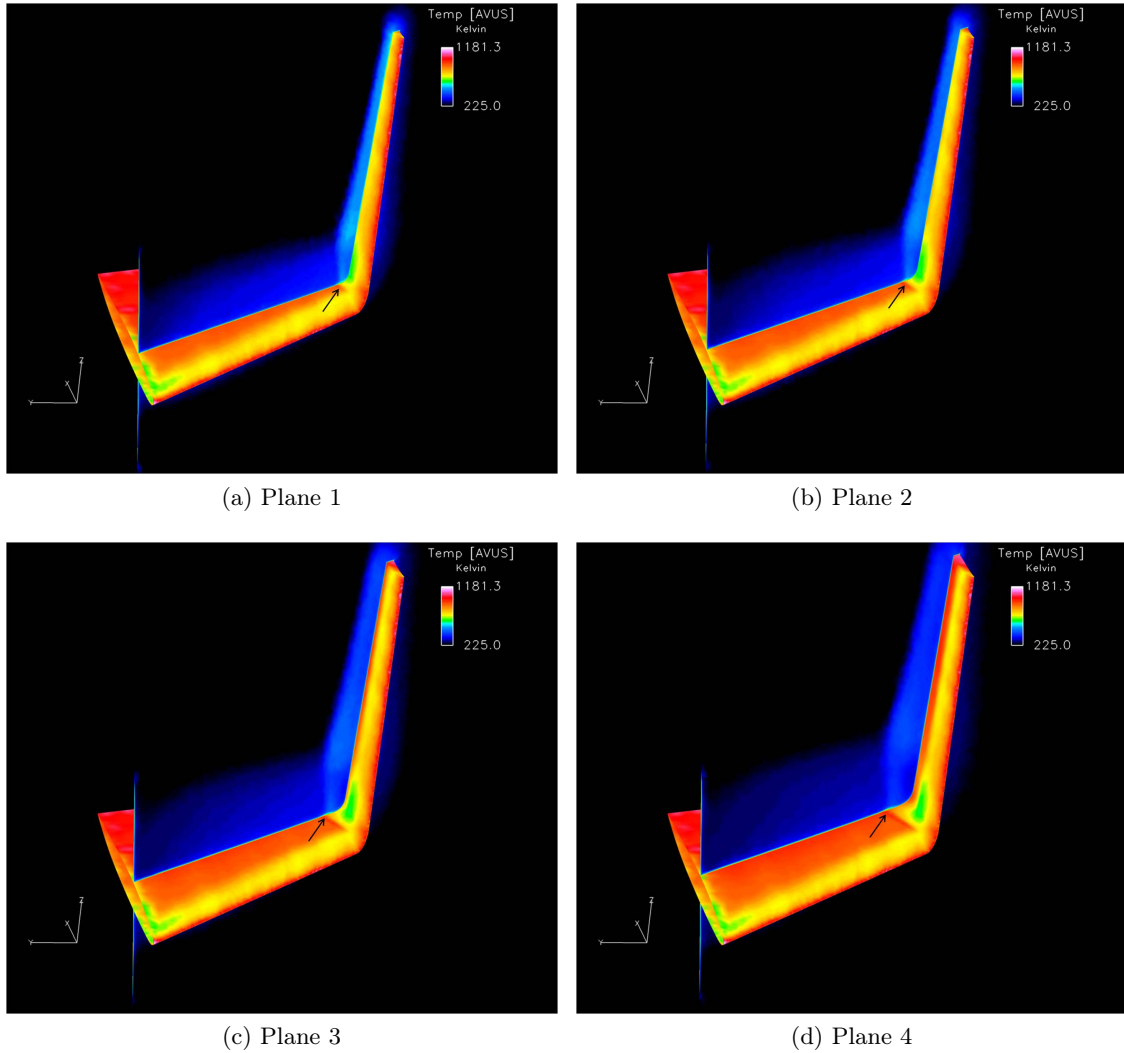


Figure 54 Combined Plane and Surface Temperature Contours, 2° , Mach 4.5

4.3 Angle of Attack for the Experiment

Upon analysis of the results, an angle of attack of 3° was recommended for the mounting angle of the experimental wing on the FL rocket for two main reasons. The first reason for this recommendation was the approximately zero coefficient of lift in the Mach 2-4.5 testing region. The plot of C_l for 3° is presented again in Figure 55 for convenience.

As part of the launch criteria the rocket needs to spin at 4Hz, so USAFA requested this zero lift angle because they want the non-experimental rocket fins to provide the necessary lift to produce the spin.

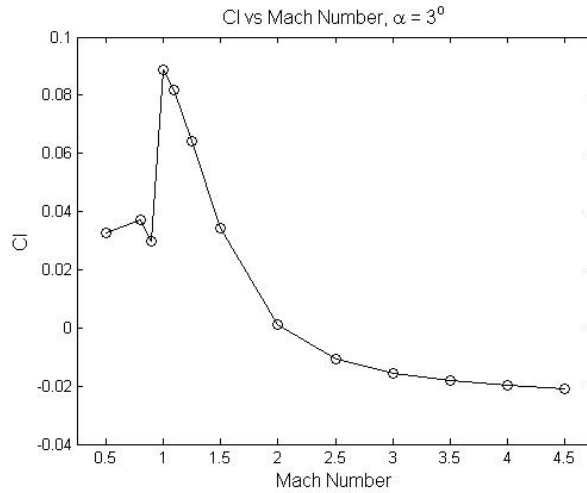


Figure 55 C_l Against Mach Number at $\alpha = 3^\circ$

Secondly, because a 3° angle of attack produces no lift it also generates minimal drag for the wing. This will make it easier for the rocket to reach high velocities required for data collection. Figure 67 presents the values of C_d as a function of Mach for the wing at 3° angle of attack. The raw coefficient data for $\alpha = 3^\circ$ is provided in Appendix G.

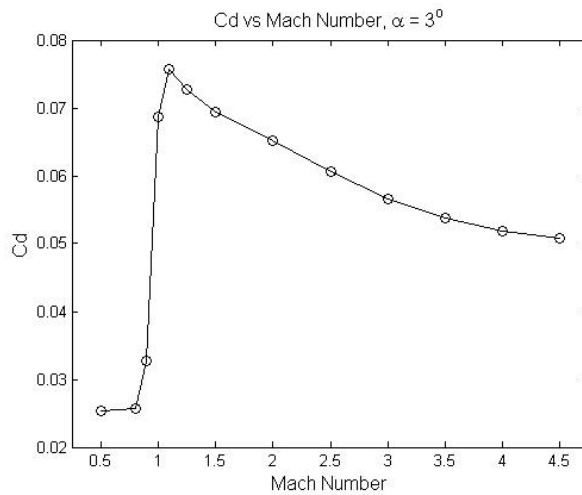
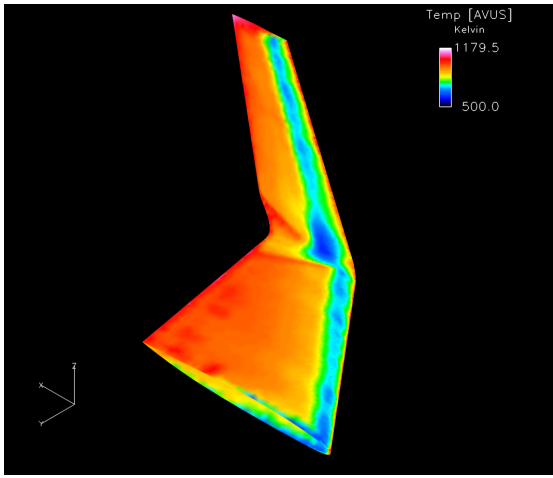


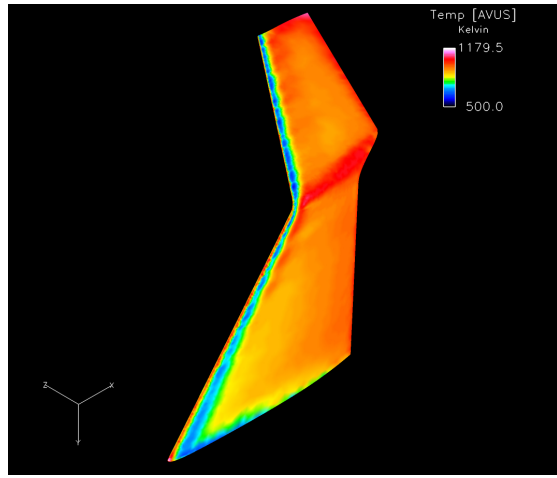
Figure 56 C_d Against Mach Number at $\alpha = 3^\circ$

4.4 Temperature Data Collection and Heating Issues

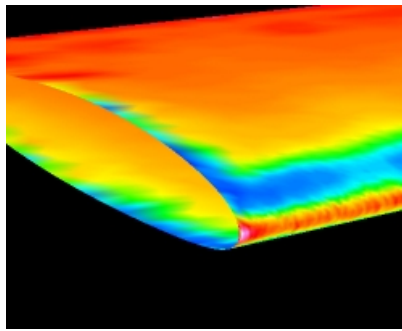
Finally due to the high temperatures and the material properties of the wing there may be data collection and possibly melting issues. Figures 57a, 57b and 57c show the temperature distribution for the 3° configuration where the high temperature areas appear in the same locations as described in Section 4.2 and reach a maximum value of 1179 K at Mach 4.5. The first issue is the temperature data collection. The temperature sensors outfitted to the wing have a maximum measurable temperature of 520 Kelvin. The temperatures in the data collection locations at the Mach 4.5 case will be on the order of 960 and 925 Kelvin for the main wing and winglet respectively. The wings will remain below 520 degrees until the rocket reaches Mach 3.0, which means the temperature sensors will be saturated for some of the data collection portion of the flight. As for the more important issue of melting, the melting point of the Aluminum the wings are made of is approximately 885 Kelvin, a temperature that will be reached between Mach 3 and 3.5. Also, the maximum temperatures seen on the wing will be 1179 Kelvin at Mach 4.5. Although the wing will be exposed to temperatures above the melting point of the wing the time of exposure will only be a few seconds.



(a) Top Surface



(b) Bottom Surface



(c) Maximum Temperature Location

Figure 57 Temperature Distribution at $\alpha = 3^\circ$

V. Conclusions and Recommendations

This Chapter contains conclusions drawn from this research study. Finally it outlines recommendations for future researchers in this area.

5.1 Conclusions

An angle of attack of 3° is the best choice for mounting the experimental wing onto the rocket. This would provide the zero lift necessary for the non-experimental wings to induce the 4Hz spin. Also this angle of attack is near the minimum drag of the wing which will help the rocket to attain a desired Mach 4.5 speed. An important point to make is that the shock shock interactions do not cause any temperature spikes on the surface of the wing. The winglet shock wave does increase the temperature of the wing, but these temperatures remain relatively low and will not effect the experiment. However, at these temperatures the temperature sensors will become saturated beginning around Mach 3.0. Also, the experimental wings will encounter temperatures higher than the melting point of the wing material. Although these temperatures will only be attained for a short period of time a high temperature coating should be used on the wings.

5.2 Recommendations and Suggestions for Future Research

5.2.1 Changes in Gridding. A large factor is this research study was the development of the grid to use in simulations. This process can be long and tedious; because of this, simplifications were made in the creation of the grid used in this research. The first of which was modeling the fuselage body as a flat plate and ignoring mountings and other physical details actually incorporated onto the rocket. For future research, modeling of the entire rocket could bring to light affects uncaptured by this simplified model. This style of modeling would provide a much better picture of the actual experiment. A well designed structured grid can yield higher orders of accuracy in the solutions; unfortunately, structured grids are more difficult to construct and would require considerably greater time to create.

In addition to gridding the physical rocket, making grids specifically designed for each flight data point would be beneficial. Only one grid was used for a large variety of Mach number and α combinations. By making a separate grid for individual cases each grid could be tailored to resolve the specific flow developed. For example, a grid designed for a high Mach case could focus on the area on the main wing in which the shock from the winglet forms, whereas a subsonic case might evenly space cells as there are no shock waves to capture. Also the prismatic cells used in this research did not completely resolve the boundary layer for every case. New grids should incorporate cells better suited for resolving the boundary layer on the wing surface particularly at the leading edge of the wing.

Finally, depending on the range of Mach numbers and altitudes in future experiments, a new code which incorporates a gas model may need to be used. While this experiment did not reach a point where a gas model was necessary, the FAST Program hopes to attain Mach 7; at these speeds air will no longer be in chemical equilibrium. The form of AVUS code used here cannot resolve these phenomenon.

5.2.2 Changes to the Experiment. One improvement to this experiment would be to locate the temperature sensors in more appropriate positions. Neither of the locations used for the temperature sensors will capture the temperature extremes the wing will experience. In future experiments, at least one temperature sensor with the ability to sense temperatures approaching 1000 K needs to be located near the wing elbow where temperatures are at a maximum. As outlined in Section 4.2 this is the region where the highest temperatures will occur due to the shock interactions. Having experimental data to verify physical temperatures in the high temperature region will aid in selecting materials for future tests.

Another modification to the experiment would be the addition of pressure sensors in the elbow region where the shock from the winglet encounters on the main wing. This would enable greater study of the effect that this shock wave has on the overall lifting characteristics of the wing. Pressure data collected at this location would show the formation and development of this shock wave and further validate the models developed in this study. Fully understanding this event would further the research base needed to develop an RBS.

VI. Appendix-A: Flight Profile Data Points

All Cases run at $\alpha = 0^\circ, 1^\circ, 2^\circ, 3^\circ, 4^\circ, 5^\circ, 6^\circ, 8^\circ, 10^\circ, 12^\circ, 14^\circ, 16^\circ, 18^\circ, 20^\circ$

| Mach Number | Altitude ft (km) | Pressure Pa | Temperature K |
|-------------|---------------------|----------------|------------------|
| 0.5 | Sea Level | 101325.0 | 288.15 |
| 0.8 | 3.5k (1.07) | 891482.5 | 281.22 |
| 0.9 | 4.5k (1.37) | 859019.7 | 279.24 |
| 1.0 | 5k (1.52) | 843125.3 | 278.24 |
| 1.1 | 5.25k (1.60) | 835214.8 | 277.75 |
| 1.25 | 5.5k (1.67) | 827416.3 | 277.25 |
| 1.5 | 6k (1.83) | 812049.2 | 276.28 |
| 2.0 | 7.5k (2.29) | 767185.4 | 273.31 |
| 2.5 | 9k (2.74) | 724285.0 | 270.32 |
| 3.0 | 10k (3.05) | 696945.0 | 268.35 |
| 3.5 | 15k (4.57) | 571819.6 | 258.43 |
| 4.0 | 20k (6.10) | 466004.2 | 248.57 |
| 4.5 | 30k (9.14) | 301482.8 | 228.81 |
| 4.0 | 35k (10.67) | 238422.9 | 218.80 |
| 3.5 | 40k (12.19) | 188226.9 | 216.66 |
| 3.0 | 50k (15.24) | 115972.6 | 216.65 |
| 2.5 | 60k (18.29) | 72313.6 | 216.66 |
| 2.0 | 70k (21.34) | 44377.5 | 217.99 |
| 1.5 | 80k (24.38) | 27830.4 | 216.66 |
| 1.0 | 100k (30.48) | 11053.2 | 232.66 |

VII. Appendix-B: Sample Job File

```

#!/bin/bash
#####
# Queue Options
#####
#PBS -l nodes=15:ppn=2
#PBS -M benjamin.switzer@afit.edu
#PBS -m abe
#PBS -j oe
#
#echo Working directory is $PFS_O_WORKDIR
cd $PBS_O_WORKDIR
#####
# Script Banner
#####
echo -e ""
echo -e "=====
echo -e " AVUS Job File Script "
echo -e "=====
#####
# AVUS - File names
#####
export GRIDNAME=Final_COBALT;
export BCNAME=Final_COBALT;
export RESULTNAME=altSL_MO5_a0_Final;
export TAPNAME=;
#####
# AVUS - File paths
#####
#export AVUSLOC=${HOME}/avus/bin;
export AVUSLOC=${HOME}/avus;
export JOBLOC=${HOME}/Thesis/Final_Job_Files/AoA_0;
export GRIDLOC=${HOME}/Thesis/GridGen_Files;
export BCLOC=${HOME}/Thesis/GridGen_Files;
export SCRATCH=${HOME}/Thesis/Final_Results/AoA_0/Case1;
export RESULTLOC=${HOME}/Thesis/Final_Results/AoA_0;
export TAPLOC=${SCRATCH};
#####
# AVUS - Executable Spec
#####
export MACHINE_ARCH="linux";      # linux | macosx | etc...
export PRECISION="double";        # single |double
#export RUNSCRIPT="avus.linux.dp"; # AvusRUN | AvusRUN_ibm
export RUNSCRIPT="AvusRUN";      # AvusRUN | AvusRUN_ibm
#####

# MPI - Run command
#####
export RUN="mpirun"
#####
# Clean scratch directory
cd $SCRATCH/
rm -f avus AvusIN* AvusOUT* fort.* *.shutdown
#####
cat > $SCRATCH/$RESULTNAME.inp << EOF
*****
                TITLE
*****
Wing Sea Level M 0.5 AoA 0
*****
                INPUT FILE CONTROL PARAMETERS
*****
START OPTION (1=INITIAL RUN, 2=RESTART, 3=RESTART & RECALC WALL DIST)

```

```

NO. PROCESSORS      GRID & INTERSECTION FILE FORMAT (0=UNIFORM, 1=FORM)
 28  0
SPLITTING PROCS    PROVIDE FLOW DATA? (0=NO,1-11=YES)
-1  0
*****
                OUTPUT FILE CONTROL PARAMETERS
*****
CREATE PICTURE FILE? (0=NO,1-9=YES)  FORMAT(0=UNIFORM, 1=FORM)
 0  0
CONVERGENCE FREQ.      RESTART FREQ.  MOVIE TAP FREQ.  PIX FREQ.
 25  -1  -1  -1  -1
*****
                ALGORITHM PARAMETERS
*****
EQUATION SET (1=EULER, 2=LAMINAR N-S, 3=TURBULENT N-S)
 3
TURBULENCE MODEL (1=SPALART,2=Spalart-DES,3=MentorBSL,4=MentorSST,5=WilcoxKW,6=WilcoxSST)
 1
SPATIAL ACCURACY (1 OR 2)  TEMPORAL ACCURACY (1 OR 2)
 1  1
THETA (0.5-1.0)
 1.00
RHS IFLUX(1=G&G,2=ROE,3=HLLC,4=VLEER) LSTSQ.WTS(0=OFF,1=ON) LIMITER(0=OFF,1=B&J,2=Venk)
 1  0  2
ITERATIVE MATRIX SOLUTION SCHEME (1=JACOBI, 2=GAUSS-SEIDEL)
 2
NO. ITERATIONS (SWEEPS) OF ABOVE MATRIX SOLUTION SCHEME
 32
INVISCID JACOBIAN DDF      VISCOUS JACOBIAN DDF
 0.1  0.1
CFL      TIME STEPS      NEWTON SUB-ITERATIONS
1.e+6    5000            0
TIME ACCURATE?      REQUESTED TIME STEP
 0  -1.
*****
                REFERENCE CONDITIONS & PHYSICAL CONSTANTS
*****
UNITS (1=MKS, 2=CGS, 3=FOOT-SLUG-SEC, 4=INCH-SNAIL-SEC)
 2
MACH NO.  ANGLE OF ATTACK  ANGLE OF SIDESLIP
 0.5  0.0  0.0
STATIC PRESSURE  STATIC TEMPERATURE
 1013250.0  288.15
GAMMA  GAS CONSTANT  PRANDTL NUMBER  GRAVITY
-1.  -1.  -1.  0.
*****
                INITIAL CONDITIONS
*****
MACH NO.  ANGLE OF ATTACK  ANGLE OF SIDESLIP
 0.5  -370.  -370.
STATIC PRESSURE  STATIC TEMPERATURE
-1.  -1.
TURBULENT KINEMATIC VISCOSITY RATIO
-1.  -1.
*****
                GEOMETRY PARAMETERS
*****
COORDINATE SYSTEM (1=FLO57, 2=PANAIR, 3=AXI-SYMMETRIC)
 2
AXISYMMETRIC FORCE ACCOUNTING
-1
REFERENCE AREA
 416.1343476
X,Y,Z COORDINATES OF MOMENT REFERENCE POINT
 668.665775 -249.9355 -29.58783

```

```

REFERENCE LENGTHS FOR MOMENTS ABOUT X-,Y- AND Z-AXIS
1.0 1.0 1.0
*****
END OF INPUT INFORMATION
*****
EOF

cp -p $SCRATCH/$RESULTNAME.inp $JOBLOC/$RESULTNAME.inp.out

#-----
# AvusRUN script argument list:
#
# 1 - AVUS input file name
# 2 - AVUS output file name
# 3 - precision switch
# 4 - grid file name
# 5 - old restart file name
# 6 - new restart file name
# 7 - picture file name
# 8 - tap location file name
# 9 - shutdown file name
# 10 - performance file
# 11 - bl trip file name
# 12 - bc file name
# 13 - overwrite flag
# 14 - machine type
# 15 - '-mdiceargs' (optional:only when run from MDICE)
# 16 - string of mdice args (optional:only when run from MDICE)
#-----
# Available precision:
# single, double
#
# Available machine types:
# ibm,sgi,t3e
#-----
#
#
$AVUSLOC/$RUNSCRIPT \
$SCRATCH/$RESULTNAME.inp \
$RESULTLOC/$RESULTNAME.out \
$PRECISION \
$GRIDLOC/$GRIDNAME.grd \
$SCRATCH/junk.intr \
$RESULTLOC/$RESULTNAME.rst \
$JOBLOC/$RESULTNAME.trst \
$RESULTLOC/$RESULTNAME.pix \
$SCRATCH/$JOBNAME.tap \
$JOBLOC/$RESULTNAME.shutdown \
$SCRATCH/$RESULTNAME.movtap \
$SCRATCH/ramp.trip \
$BCLOC/$BCNAME.bc \
overwrite \
$MACHINE_ARCH \

```

VIII. Appendix-C: Navier-Stokes Equations

Equation (4) shows the Navier-Stokes equation in integral form, where Ω is an arbitrary control volume, \vec{W} is the vector of conservative variables, and \vec{F}_c and \vec{F}_v are the vectors of convective and viscous fluxes respectively.

$$\frac{\partial}{\partial t} \int_{\Omega} \vec{W} d\Omega + \oint_S (\vec{F}_c - \vec{F}_v) dS = 0 \quad (4)$$

The vector, \vec{W} , represents the three dimensional conservative variables consisting of the five terms given by Equation (5). The first term, ρ , is the quantity preserved by the conservation of mass equation. The next three terms, ρu , ρv , and ρw , designate momentum in the x , y , and z directions and are preserved by the conservation of momentum equations. The last term, ρE , represents both the internal and kinetic energies and is preserved by the conservation of energy equation.

$$\vec{W} = \begin{bmatrix} \rho \\ \rho u \\ \rho v \\ \rho w \\ \rho E \end{bmatrix} \quad (5)$$

The vector of convective fluxes, denoted by \vec{F}_c , is given in Equation (6). The variable V is the contravariant velocity, or the velocity normal to the surface element dS , and is given by Equation (7) and H is total enthalpy given by Equation (8).

$$\vec{F}_c = \begin{bmatrix} \rho V \\ \rho u V + n_x P \\ \rho v V + n_y P \\ \rho w V + n_z P \\ \rho H V \end{bmatrix} \quad (6)$$

$$V = n_x u + n_y v + n_z w \quad (7)$$

$$H = E + \frac{P}{\rho} \quad (8)$$

The vector of viscous fluxes, denoted by \vec{F}_v , is given in Equation (9).

$$\vec{F}_v = \begin{bmatrix} 0 \\ n_x \tau_{xx} + n_y \tau_{xy} + n_z \tau_{xz} \\ n_x \tau_{yx} + n_y \tau_{yy} + n_z \tau_{yz} \\ n_x \tau_{zx} + n_y \tau_{zy} + n_z \tau_{zz} \\ n_x \Theta_x + n_y \Theta_y + n_z \Theta_z \end{bmatrix} \quad (9)$$

Where Θ_x , Θ_y , and Θ_z describe the work of the viscous stresses and of the heat conduction in the fluid and are given in Equations (10) - (12).

$$\Theta_x = u\tau_{xx} + v\tau_{xy} + w\tau_{xz} + k\frac{\partial T}{\partial x} \quad (10)$$

$$\Theta_y = u\tau_{yx} + v\tau_{yy} + w\tau_{yz} + k\frac{\partial T}{\partial y} \quad (11)$$

$$\Theta_z = u\tau_{zx} + v\tau_{zy} + w\tau_{zz} + k\frac{\partial T}{\partial z} \quad (12)$$

Where τ is the stress tensor, k is the thermal conductivity, and T is temperature[20][21].

IX. Appendix-D: Spalart Allmaras Turbulence Model Equations

The governing equation of the Spalart-Allmaras model, given by Equation (13), uses a working variable, $\bar{\nu}$, related to eddy viscosity, ν_t through Equation (14).

$$\begin{aligned} \frac{d\bar{\nu}}{dt} = \frac{3}{2} [\nabla \cdot ((\nu + \bar{\nu})\nabla\bar{\nu}) + 0.622(\nabla\bar{\nu})^2] + 0.1355\bar{S}\bar{\nu}(1 - f_{t2}) \\ - [3.239f_w - 0.806f_{t2} \left[\frac{\bar{\nu}}{d}\right]^2 + f_{t1}(\nabla q)^2] \end{aligned} \quad (13)$$

$$\nu_t = \bar{\nu}f_{v1} \quad (14)$$

The various functions in Equation (2) are defined in Equations (15) - (18) where d is the distance to the wall, κ is the von Karman constant, d_t is the distance from a field point to the surface, ω_t is the vorticity at the surface, Δq is the difference in velocity between the field point and the surface, and g_t is the minimum of 1.0 or $\Delta q\omega_t\Delta x$ where Δx is the grid spacing along the wall at the surface.

$$f_{t1} = g_t e^{\left[-2\left(\frac{\omega_t}{\Delta q}\right)^2 (d^2 + g_t^2 d_t^2)\right]} \quad (15)$$

$$f_{t2} = 1.1e^{(-2.0\chi^2)} \quad (16)$$

Where χ is $\frac{\bar{\nu}}{\nu}$.

$$\bar{S} = \frac{\partial v}{\partial x} - \frac{\partial u}{\partial y} + \frac{\bar{\nu}}{\kappa^2 d^2} \left(1 - \frac{\chi}{1 + \chi \left(\frac{\chi^3}{\chi^3 + 7.13}\right)}\right) \quad (17)$$

$$f_w = (r + 0.3(r^6 - r)) \left(\frac{65}{(r + 0.3(r^6 - r))^6 + 64}\right)^{\frac{1}{6}} \quad (18)$$

Where r is $\frac{\bar{\nu}}{5\kappa^2 d^2}$ [22].

X. *Appendix-E: Gottlieb and Groth Riemann Solver*

The governing equation for the Gottlieb and Groth Riemann Solver is given in Equation (19) where l and r represent properties to the left and right of the contact and the prime denotes differentiation with respect to u^* .

$$u_{i+1}^* = u_i^* - \frac{P_l^*(u_i^*) - P_r^*(u_i^*)}{P_l^{*'}(u_i^*) - P_r^{*'}(u_i^*)} \quad (19)$$

The necessary equations for leftward and rightward moving shock waves are given in Equations (20) through (23) where $M_{l,r}$ is the shock Mach number.

$$M_{l,r} = \frac{\gamma_{l,r} + 1}{4} \frac{u^* - u_{l,r}}{a_{l,r}} - \left[1 + \left(\frac{\gamma_{l,r} + 1}{4} \frac{u^* - u_{l,r}}{a_{l,r}} \right)^2 \right]^{\frac{1}{2}} \quad (20)$$

$$P_{l,r}^* = P_{l,r} + \frac{\gamma_{l,r} P_{l,r}}{a_{l,r}} (u^* - u_{l,r}) M_{l,r} \quad (21)$$

$$P_{l,r}^{*'} = \frac{2 \gamma_{l,r} P_{l,r} M_{l,r}^3}{1 + M_{l,r}^2} \quad (22)$$

$$a_{l,r}^* = a_{l,r} \left[\frac{(\gamma_{l,r} + 1) + (\gamma_{l,r} - 1) \frac{P_{l,r}^*}{P_{l,r}}}{(\gamma_{l,r} + 1) + (\gamma_{l,r} - 1) \frac{P_{l,r}}{P_{l,r}^*}} \right]^{\frac{1}{2}} \quad (23)$$

The necessary equations for left and right expansion waves are given in Equations (24) through (27) .

$$a_{l,r}^* = a_{l,r} - \frac{\gamma_{l,r} - 1}{2} (u^* - u_{l,r}) \quad (24)$$

$$P_{l,r}^* = P_{l,r} \left[\frac{a_{l,r}^*}{a_{l,r}} \right]^{\frac{2\gamma_{l,r}}{\gamma_{l,r} - 1}} \quad (25)$$

$$P_l^{*'} = \frac{-\gamma_l P_l^*}{a_l^*} \quad (26)$$

$$P_r^{*'} = \frac{\gamma_r P_r^*}{a_r^*} \quad (27)$$

At the beginning of the solution an initial guess for the flow velocity u_o^* is obtained from Equation (28).

$$u_o^* = \frac{\left(u_l + \frac{2}{\gamma_l - 1} a_l\right) c + \left(u_l + \frac{2}{\gamma_l - 1} a_l\right)}{1 + c} \quad (28)$$

The variable, c , is given by Equation (29), where σ equals γ_l if $P_l \geq P_r$ or γ_r if $P_l < P_r$ [23].

$$c = \frac{\gamma_l - 1}{\gamma_r - 1} \frac{a_r}{a_l} \left[\frac{P_l}{P_r} \right]^{\frac{\sigma - 1}{2\sigma}} \quad (29)$$

XI. Appendix-F: C_l vs Mach Number Plots

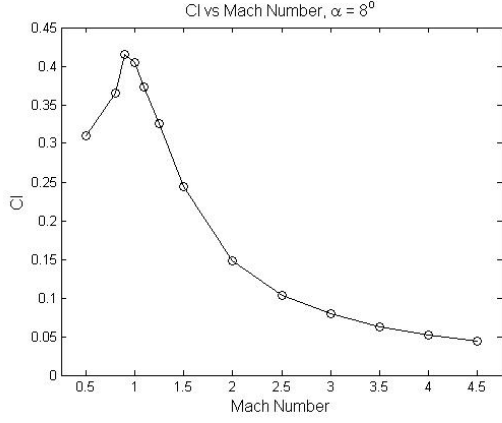


Figure 58 C_l vs Mach Number $\alpha = 8^\circ$

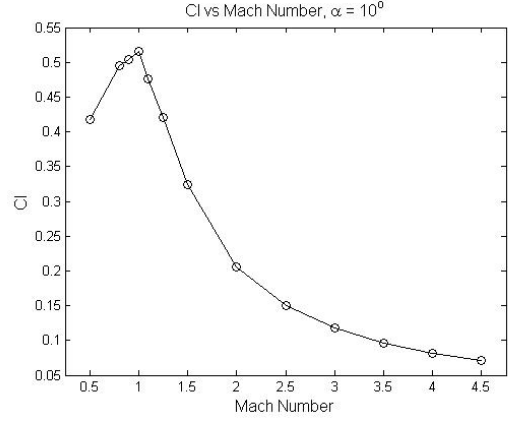


Figure 59 C_l vs Mach Number $\alpha = 10^\circ$

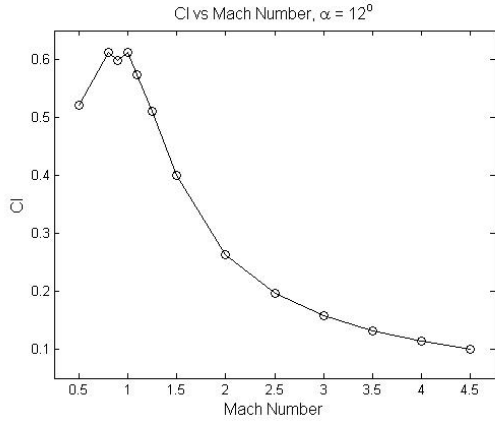


Figure 60 C_l vs Mach Number $\alpha = 12^\circ$

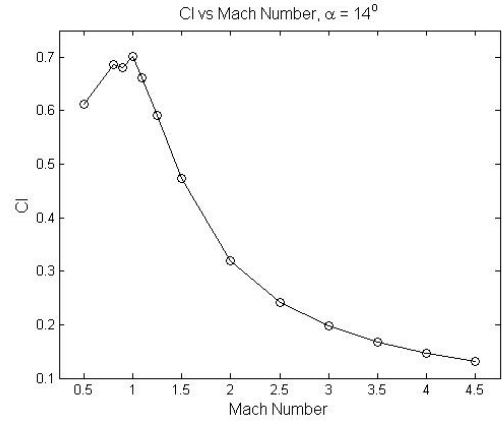


Figure 61 C_l vs Mach Number $\alpha = 14^\circ$

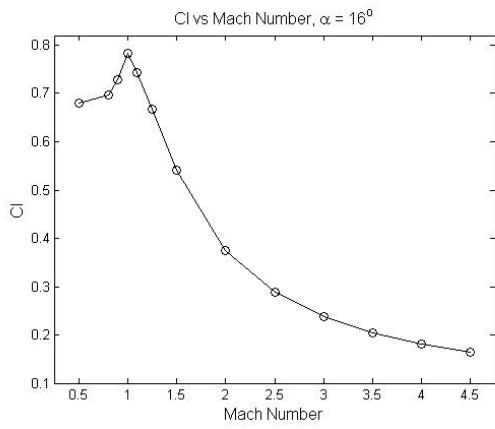


Figure 62 C_l vs Mach Number $\alpha = 16^\circ$

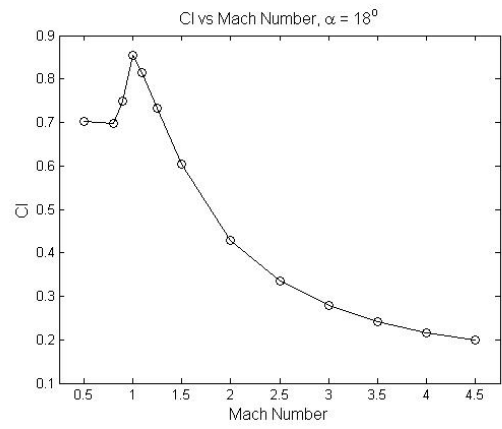


Figure 63 C_l vs Mach Number $\alpha = 18^\circ$

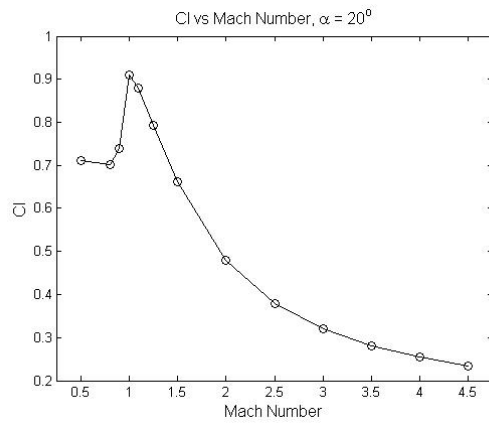


Figure 64 C_l vs Mach Number $\alpha = 20^\circ$

XII. Appendix-G: C_d vs Mach Number Plots

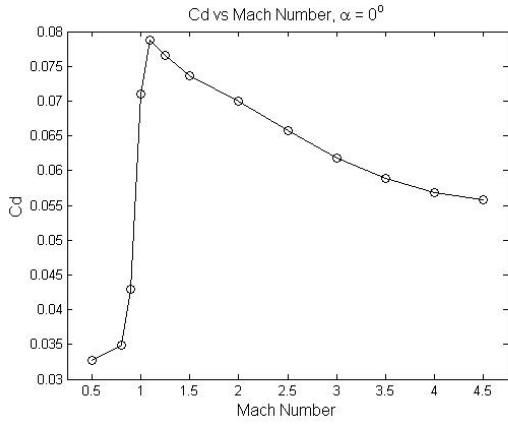


Figure 65 C_d vs Mach Number $\alpha = 3^\circ$

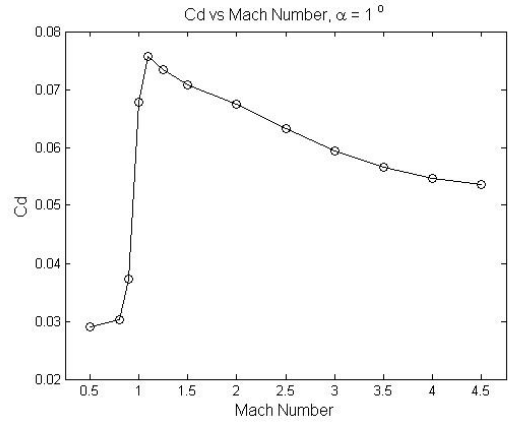


Figure 66 C_d vs Mach Number $\alpha = 4^\circ$

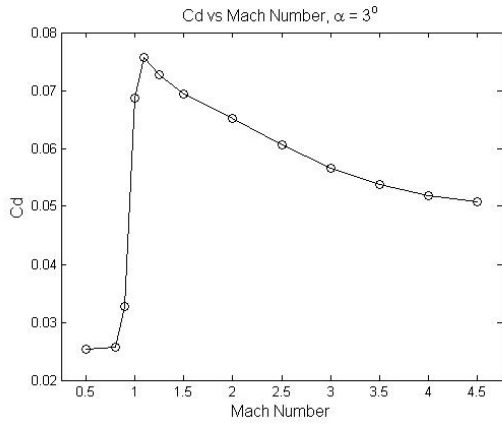


Figure 67 C_d vs Mach Number $\alpha = 3^\circ$

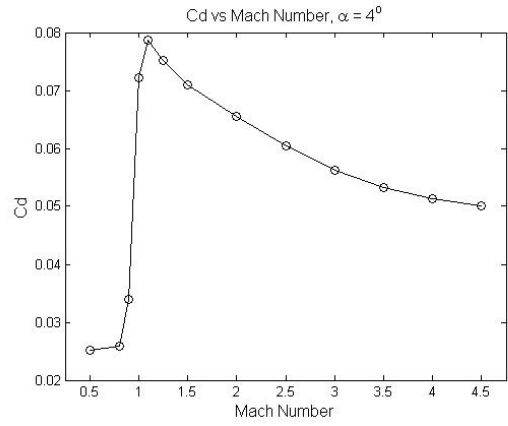


Figure 68 C_d vs Mach Number $\alpha = 4^\circ$

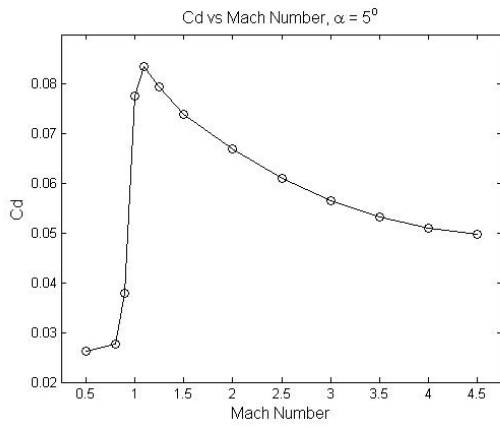


Figure 69 C_d vs Mach Number $\alpha = 5^\circ$

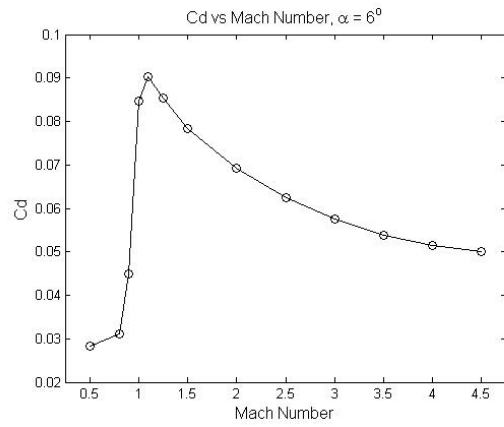


Figure 70 C_d vs Mach Number $\alpha = 6^\circ$

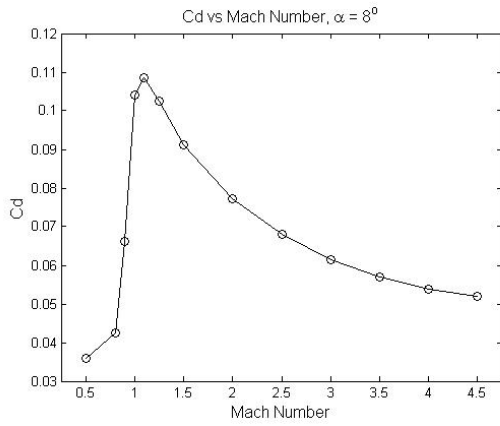


Figure 71 C_d vs Mach Number $\alpha = 8^\circ$

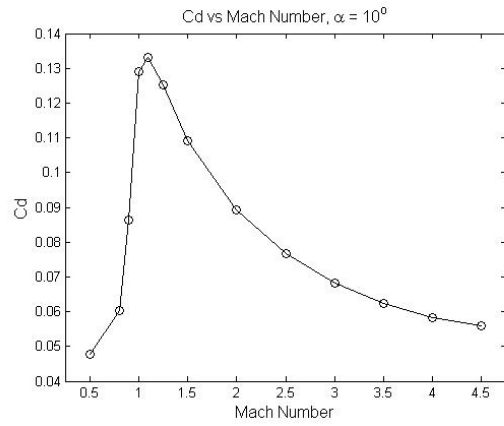


Figure 72 C_d vs Mach Number $\alpha = 10^\circ$

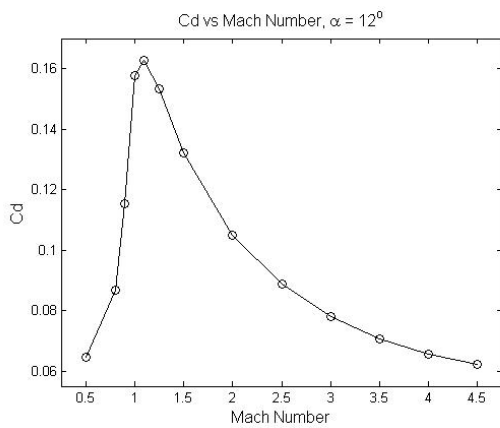


Figure 73 C_d vs Mach Number $\alpha = 12^\circ$

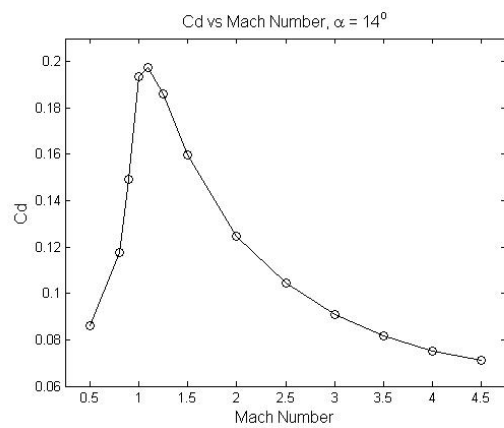


Figure 74 C_d vs Mach Number $\alpha = 14^\circ$

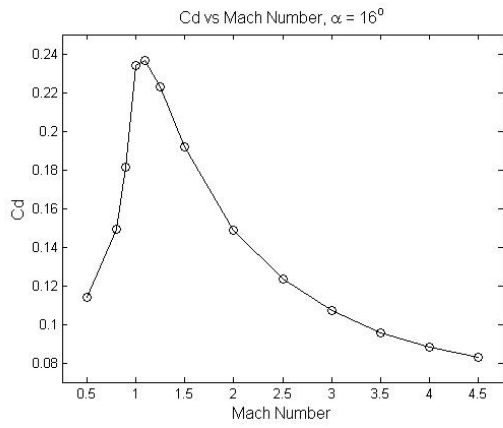


Figure 75 C_d vs Mach Number $\alpha = 16^\circ$

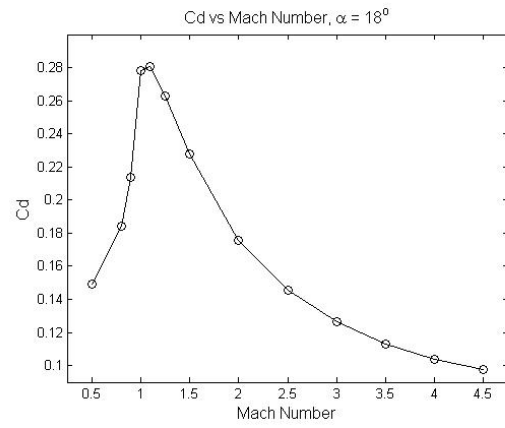


Figure 76 C_d vs Mach Number $\alpha = 18^\circ$

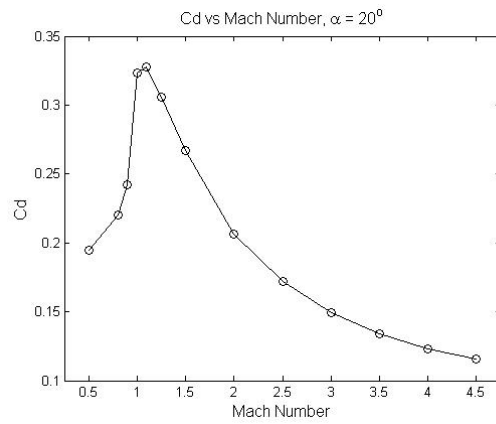


Figure 77 C_d vs Mach Number $\alpha = 20^\circ$

XIII. Appendix-H: Raw Coefficient Data for 3° Angle of Attack

| Case | Cl | Cd | Cm(Pitch) | Cm(Yaw) | Cm(Roll) |
|---------|-----------|----------|-----------|----------|-----------|
| SL | 0.032624 | 0.025350 | 0.162270 | 1.498800 | -0.732140 |
| 3.5kft | 0.037068 | 0.025758 | 0.174330 | 1.660300 | -0.907140 |
| 4.5kft | 0.029615 | 0.032666 | 0.411670 | 1.816500 | -0.913660 |
| 5kft | 0.088752 | 0.068607 | -0.358310 | 3.126200 | -1.496700 |
| 5.25kft | 0.081715 | 0.075724 | -0.269610 | 3.429500 | -1.352800 |
| 5.5kft | 0.064124 | 0.072788 | -0.162410 | 2.852600 | -0.826130 |
| 6kft | 0.034279 | 0.069401 | 0.132300 | 1.869300 | -0.025722 |
| 7.5kft | 0.001169 | 0.065093 | 0.489580 | 0.921200 | 0.702890 |
| 9kft | -0.010868 | 0.060577 | 0.576260 | 0.649210 | 0.839100 |
| 10kft | -0.015623 | 0.056648 | 0.585720 | 0.555380 | 0.835800 |
| 15kft | -0.018209 | 0.053814 | 0.584950 | 0.502850 | 0.819770 |
| 20kft | -0.019879 | 0.051901 | 0.583850 | 0.465680 | 0.807080 |
| 30kft | -0.020942 | 0.050839 | 0.581740 | 0.444330 | 0.795580 |
| 35kft | -0.019810 | 0.052771 | 0.585750 | 0.475950 | 0.808170 |
| 40kft | -0.018118 | 0.055489 | 0.588840 | 0.522140 | 0.821760 |
| 50kft | -0.015550 | 0.059856 | 0.595110 | 0.590380 | 0.841580 |
| 60kft | -0.010948 | 0.065202 | 0.593470 | 0.693750 | 0.851650 |
| 70kft | 0.000662 | 0.071184 | 0.517200 | 0.969040 | 0.724970 |
| 80kft | 0.032707 | 0.077535 | 0.179800 | 1.894300 | 0.023954 |
| 100kft | 0.084670 | 0.083650 | -0.338870 | 3.051000 | -1.264100 |

Bibliography

1. Picture of the Proposed X-20 Aircraft. Internet picture accessed 4 Jan. 2010 from <http://www.ascho.wpafb.af.mil/start/PHOTOS/PG26-A.JPG>.
2. Picture of the Conceptual Design of the Blackswift Test Bed. Internet picture accessed 4 Jan. 2010 from http://www.airforcetimes.com/news/2008/09/airforce_blackswift_092208w/%+.
3. HIFiRE 0 Launch on May 7, 2009. Internet picture accessed 15 Jan. 2010 from <http://www.uq.edu.au/hypersonics/?page=19501>.
4. Hellman, B., McKee, K., Street, M., and Remillard, C., 2009. "Advancing ORS Technologies and Capabilities with a Space Tourist Suborbital Vehicle." In AIAA SPACE 2009 Conference and Exposition.
5. Proposed Flight Profile for Virgin Galactics SpaceShipTwo Vehicle. Internet picture accessed 5 Jan. 2010 from <http://www.virgingalactic.com/overview/environment/>.
6. Bertin, J. J., 1994. *Hypersonic Aerothermodynamics* American Institute of Aeronautics and Astronautics, Washington, D.C.
7. Houchin, R. F., 2006. *US Hypersonic Research and Development - The Rise and Fall of Dyna-Soar (1944-1963)*, First ed. Routledge, 270 Madison Avenue, New York, NY 10016.
8. McMillan, B. Review of the Air Force Space Research and development Program. Letter to Secretary of Defense McNamara, June 1963.
9. Kempel, R., Painter, W., and Thompson, M., 1994. Developing and Flight Testing the HL-10 Lifting Body: A Precursor to the Space Shuttle. Reference Publication 1332, NASA, April.
10. Picture of the HL-10 Aircraft. Internet picture accessed 5 Jan. 2010 from <http://www.dfrc.nasa.gov/Gallery/Photo/HL-10/Small/ECN-1289.jpg>.
11. Picture of the M2-F2 Aircraft. Internet picture accessed 15 Jan. 2010 from http://commons.wikimedia.org/wiki/File:Northrop_M2-F2.jpg.
12. DARPA FALCON (Force Application and Launch from CONUS) Technology Demonstration Program Fact Sheet. On the WWW, at http://www.darpa.mil/news/2003/falcon_fs.pdf, November 2003 PDF file.
13. DARPA Falcon Technology Demonstration Program HTV-3X Blackswift Test Bed. On the WWW, at <http://www.darpa.mil/Docs/Falcon-Blackswift%20FS%20Oct08.pdf>, October 2008 PDF file.
14. Dolvin, D. J., 2008. "Hypersonic International Flight Research and Experimentation (HIFiRE) Fundamental Sciences and Technology Development Strategy." In 15th AIAA/AAAF International Conference: Space Planes and Hypersonic Systems and Technologies.

15. J. Odam, A. Paull, H. A. D. H. R. P. R. P., 2009. "HIFiRE 0 Flight Test Data." In 16th AIAA/DLR/DGLR International Space Planes and Hypersonic Systems and Technologies Conference.
16. Galactic, V. Virgin Galactic Unveils SpaceShipTwo, the World's First Commercial Manned Spaceship. On the WWW, at <http://www.scaled.com/news/VGPressRelease12-07-09.pdf>, December 2009 PDF file.
17. Simmons, J. R., 2009. "Aeroelastic Optimization of Sounding Rocket Fins." MS Thesis, Air Force Institute of Technology Graduate School of Engineering and Management, Wright-Patterson AFB, OH 45431. AFIT/GSS/ENY/09-J02.
18. Gridgen, 2005. *Gridgen Users Manual*, version 15 ed.
19. Air Force Research Laboratory CFD Research Branch, 2005. *Air Vehicles Unstructured Solver (AVUS) User's Manual*.
20. Blazek, J., 2005. *Computational Fluid Dynamics: Principles and Applications*, Second ed. ELSEVIER Ltd, Kidlington, Oxford, UK.
21. John D. Anderson, J., 2007. *Fundamentals of Aerodynamics*, Fourth ed. McGraw-Hill, New York, NY.
22. Hoffmann, K. A., and Chiang, S. T., 2000. *Computational Fluid Dynamics: Volume III*, Fourth ed. Engineering Education System, Wichita, KS.
23. Gottlieb, J. J., and Groth, C. P. T., 1988. "Assessment of Riemann Solvers for Unsteady One-Dimensional Inviscid Flows of Perfect Gases." *Journal of Computational Physics*, **78**, pp. 437–458.
24. Vinacco, M. J., 2010. "ExFiT Flight Design and Structural Modeling for Falcon-LAUNCH VIII Sounding Rocket." MS Thesis, Air Force Institute of Technology Graduate School of Engineering and Management, Wright-Patterson AFB, OH 45431. AFIT/GAE/ENY/10-M27.
25. John D. Anderson, J., 2006. *Hypersonic and High-Temperature Gas Dynamics*, Second ed. American Institute of Aeronautics and Astronautics, Reston, VA.

Vita

Second Lieutenant Benjamin P. Switzer graduated from Rockbridge County High School in Virginia in 2004 and pursued an undergraduate degree at the Virginia Military Institute. Graduating with a Bachelor of Science in Mechanical Engineering, he was commissioned into the US Air Force and was married to his wife in May of 2008. As his first assignment, he was selected to attend AFIT and arrived in August of the same year. Lt Switzer completed AFIT with a Master's Degree in Aeronautical Engineering in March of 2010. Upon graduating, Lt Switzer has since been assigned to the Sustainment Depot at Robins AFB, GA. In the fall of 2010, Lt Switzer and his wife will be expecting the birth of their first child.

| REPORT DOCUMENTATION PAGE | | | | <i>Form Approved</i> OMB No. 074-0188 | |
|--|-------------------------|--|---|--|--|
| <p>The public reporting burden for this collection of information is estimated to average 1 hour per response, including the time for reviewing instructions, searching existing data sources, gathering and maintaining the data needed, and completing and reviewing the collection of information. Send comments regarding this burden estimate or any other aspect of the collection of information, including suggestions for reducing this burden to Department of Defense, Washington Headquarters Services, Directorate for Information Operations and Reports (0704-0188), 1215 Jefferson Davis Highway, Suite 1204, Arlington, VA 22202-4302. Respondents should be aware that notwithstanding any other provision of law, no person shall be subject to a penalty for failing to comply with a collection of information if it does not display a currently valid OMB control number.</p> <p>PLEASE DO NOT RETURN YOUR FORM TO THE ABOVE ADDRESS.</p> | | | | | |
| 1. REPORT DATE 25-03-2010 | | 2. REPORT TYPE Master's Thesis | | 3. DATES COVERED (From - To) Sept 2008 - Mar 2010 | |
| 4. TITLE AND SUBTITLE CFD Analysis of Experimental Wing and Winglet for FalconLAUNCH 8 and the ExFIT Program | | | | 5a. CONTRACT NUMBER | |
| | | | | 5b. GRANT NUMBER | |
| | | | | 5c. PROGRAM ELEMENT NUMBER | |
| 6. AUTHOR(S) Switzer, Benjamin P., 2d Lt, USAF | | | | 5d. PROJECT NUMBER | |
| | | | | 5e. TASK NUMBER | |
| | | | | 5f. WORK UNIT NUMBER | |
| 7. PERFORMING ORGANIZATION NAME(S) AND ADDRESS(S) Air Force Institute of Technology Graduate School of Engineering and Management (AFIT/ENY) 2950 Hobson Way, Building 640 WPAFB OH 45433-8865 | | | | 8. PERFORMING ORGANIZATION REPORT NUMBER AFIT/GAE/ENY/10-M25 | |
| 9. SPONSORING/MONITORING AGENCY NAME(S) AND ADDRESS(ES) Mr. Barry Hellman Air Force Research Laboratory Air Vehicles Directorate 2130 8TH ST B20045 R261 Wright-Patterson AFB, OH 45433 | | | | 10. SPONSOR/MONITOR'S ACRONYM(S) | |
| | | | | 11. SPONSOR/MONITOR'S REPORT NUMBER(S) | |
| 12. DISTRIBUTION/AVAILABILITY STATEMENT APPROVED FOR PUBLIC RELEASE; DISTRIBUTION UNLIMITED. | | | | | |
| 13. SUPPLEMENTARY NOTES | | | | | |
| 14. ABSTRACT Reusable launch vehicles have many benefits over their expendable counterparts. These benefits range from cost reductions to increased functionality of the vehicles. Further research is required in the development of the technology necessary for reusable launch vehicles to come to fruition. The Air Force Institute of Technology's future involvement in the ExFIT program will entail designing and testing of a new wing tip mounted vertical stabilizer in the hypersonic regime. One proposed venue for experimentation is to utilize the United States Air Force Academy's FalconLAUNCH Program which annually designs, builds, and launches a sounding rocket capable of reaching hypersonic speeds. In the Spring of 2010 an experimental wing geometry will be flown on FalconLAUNCH VIII for the ExFIT Program. The following study outlines the Computational Fluid Dynamics analysis used to determine lift and drag characteristics as well as temperature distributions of the wing geometry before testing to produce a successful launch. A majority of this analysis focused on the effects caused by shock waves forming on the winglet and their impact on the lifting characteristics and temperature distribution of the wing. Ultimately a recommendation of a 3° angle of attack is given for the experimental wings on the rocket. At this configuration the lift and drag generated by the experimental wings will be at a minimum allowing for greater stability and speed throughout the flight of the rocket. | | | | | |
| 15. SUBJECT TERMS hypersonic flight test; experimental fin tip; falconlaunch; reusable launch vehicles | | | | | |
| 16. SECURITY CLASSIFICATION OF: | | | 17. LIMITATION OF ABSTRACT UU | 18. NUMBER OF PAGES 84 | 19a. NAME OF RESPONSIBLE PERSON LtCol Ronald Simmons, AFIT/ENY |
| a. REPORT U | b. ABSTRACT U | c. THIS PAGE U | | | 19b. TELEPHONE NUMBER (Include area code) 937-255-3636 x 4723 |